The Astrophysical Journal, 909:151 (16pp), 2021 March 10 https://doi.org/10.3847/1538-4357/abd4e0
© 2021. The American Astronomical Society. All rights reserved.

Circumgalactic Mg II Emission from an Isotropic Starburst Galaxy Outflow Mapped by KCWI

Joseph N. Burchett[1,2], Kate H. R. Rubin[3,4], J. Xavier Prochaska[1,5], Alison L. Coil[4], Ryan Rickards Vaught[4], and Joseph F. Hennawi[6]
[1] University of California Observatories—Lick Observatory, University of California, Santa Cruz, CA 95064, USA; jnb@nmsu.edu
[2] New Mexico State University, Department of Astronomy, Las Cruces, NM 88001, USA; em1
[3] San Diego State University, Department of Astronomy, San Diego, CA 92182, USA
[4] Center for Astrophysics and Space Sciences, Department of Physics, University of California, San Diego, 9500 Gilman Drive, La Jolla, CA 92093, USA
[5] Kavli Institute for the Physics and Mathematics of the Universe, 5-1-5 Kashiwanoha, Kashiwa, 277-8583, Japan
[6] Department of Physics, Broida Hall, University of California at Santa Barbara, Santa Barbara, CA 93106, USA
Received 2020 May 5; revised 2020 December 12; accepted 2020 December 16; published 2021 March 12

Abstract

We present spatially resolved spectroscopy from the Keck Cosmic Web Imager (KCWI) of a star-forming galaxy at $z = 0.6942$, which shows emission from the Mg II $\lambda\lambda$2796, 2803 doublet in the circumgalactic medium (CGM) extending ∼37 kpc at 3σ significance in individual spaxels (1σ detection limit 4.8×10^{-19} erg s^{-1} cm^{-2} arcsec^{-2}). The target galaxy, selected from a near-UV spectroscopic survey of Mg II line profiles at $0.3 < z < 1.4$, has a stellar mass $\log(M_*/M_\odot) = 9.9$, a star formation rate of 50 $M_\odot$ yr^{-1}, and a morphology indicative of a merger. After deconvolution with the seeing, we obtain 5σ detections of Mg II line emission extending for ∼31 kpc measured in 7-spaxel (1.1 arcsec^2) apertures. Spaxels covering the galaxy stellar regions show clear P Cygni−like emission/absorption profiles, with the blueshifted absorption extending to relative velocities of $v = -800$ km s^{-1}; however, the P Cygni profiles give way to pure emission at large radii from the central galaxy. We have performed 3D radiative transfer modeling to infer the geometry and velocity and density profiles of the outflowing gas. Our observations are most consistent with an isotropic outflow rather than biconical wind models with half-opening angles $\phi \leqslant 80°$. Furthermore, our modeling suggests that a wind velocity profile that decreases with radius is necessary to reproduce the velocity widths and strengths of Mg II line emission profiles at large circumgalactic radii. The extent of the Mg II emission we measure directly is further corroborated by our modeling, where we rule out outflow models with extent <30 kpc.

Unified Astronomy Thesaurus concepts: Galaxy winds (626); Starburst galaxies (1570); Circumgalactic medium (1879); Galaxy evolution (594)

1. Introduction

Simply stated, galaxy formation as we know it does not work without galactic winds. These winds are now recognized as a fundamental activity of nearly all star-forming galaxies, a generalization following from a slew of spectroscopic surveys (e.g., Pettini et al. 2001; Martin 2005; Rupke et al. 2005a; Rubin et al. 2010, 2014; Coil et al. 2011), which span the majority of cosmic time and a wide diversity of galaxy properties. Winds are revealed in these down-the-barrel galaxy spectra by the telltale signature of a systematic blueshift of gas relative to the nebular emission or stellar absorption features (Heckman et al. 2000). The offset velocities range from tens to several hundreds of kilometers per second and correlate weakly with galaxy mass and star formation rate (SFR; Martin 2005; Rupke et al. 2005b; Tremonti et al. 2007; Weiner et al. 2009; Rubin et al. 2014; Chisholm et al. 2016). The ubiquity and strength of galactic winds, coupled with signatures of gas infall, strongly suggest that such flows play an important role in regulating galaxy growth (Steidel et al. 2003; Rubin et al. 2012; Martin et al. 2012; Rubin et al. 2014).

Galactic winds have also become an essential ingredient in theoretical models of galaxy formation. Initially, winds driven by star formation feedback (e.g., supernovae) were introduced to maintain a turbulent interstellar medium (ISM; Cowie et al. 1981). Now, winds are invoked as feedback mechanisms that regulate star formation and give rise to the observed distribution of stellar mass in galaxies. Furthermore, these winds enrich the intergalactic medium (IGM) and distribute heavy elements throughout the universe (Oppenheimer & Davé 2006). While winds are a critical component in theoretical treatments, even the most sophisticated and/or idealized simulations of outflows (Fielding et al. 2017; Schneider & Robertson 2018) fail to capture all of the salient astrophysics, especially across the ∼10 Gyr duration of galaxy formation.[7] Among the many challenges these models face is a somewhat existential one: the body of galactic wind literature primarily comprises observations of *cool gas* tracers (Veilleux et al. 2020). Thus, the outflow-driving mechanism(s) must produce the observed high outflow velocities while not injecting so much thermal energy as to heat and further ionize the gas beyond the neutral or low-ionization states of the tracers (e.g., Na I, Mg II, and Fe II). Therefore, these theories demand empirical constraints to bound model parameter space and inform the wind prescriptions. Present-day scaling laws (e.g., the mass–metallicity relation; Tremonti et al. 2004) and the distribution of galaxy properties (e.g., luminosity or stellar mass; Willmer et al. 2006) offer useful targets for tuning wind parameters; however, more direct constraints on the physical properties of galactic winds are in desperate need.

To date, the majority of insight into the nature of galactic winds has been derived from absorption-line analysis. Early efforts focused on the gas kinematics, e.g., estimating outflow

[7] For an analytical treatment, see also Murray et al. (2011).

speeds, and their scaling with galaxy properties (e.g., Rupke et al. 2005a; Martin 2005; Weiner et al. 2005; Rubin et al. 2010). Models were then introduced to match the flux profiles with velocity and thereby infer aspects of the density and velocity field (e.g., Martin & Bouché 2009; Steidel et al. 2010). These models were necessarily simplistic and subject to significant uncertainties owing to various aspects of the experiment, such as (i) the down-the-barrel geometry yielding poorly constrained distances of the gas from the galaxy and (ii) accessing only a small set of ions and transitions. Estimates for the physical extent of the wind and its mass were limited to order(s)-of-magnitude uncertainty.

In the past several years, with the advent of Hubble Space Telescope (HST)/COS, new data sets spanning a wider range of ions through coverage of far-UV transitions at high spectral resolution have emerged (Heckman et al. 2015; Chisholm et al. 2016, 2017). These provide better estimates of physical conditions of the gas, including its ionization state. Adopting the reasonable ansatz that the gas is primarily ionized by the photon flux of the young stellar population driving the outflow, one may then estimate the distance to the medium. Assuming power-law density and velocity laws for the gas, these analyses suggest that the densities and covering fractions of the absorbing material decrease steeply with radius (i.e., $C_f \propto r^{-0.9}$ and $n \propto r^{-5.3}$) and that the launch radius of the flow occurs at distances $r \lesssim 100$ pc from the star-forming regions (Chisholm et al. 2016, 2017). These constraints in turn imply that the rate of outward mass flow beyond several hundred parsecs drops to near zero (Chisholm et al. 2016), and hence that these winds do not result in significant enrichment of halo gas (with the caveat that they may undergo a change in phase on larger scales).

An alternative and more direct approach to assessing the radial density profile of winds is to image it in emission. Due to the overall low density of the material, the vast majority of studies pursuing this measurement have targeted nearby starbursting systems in narrowband imaging or IFU surveys of collisionally excited transitions in the optical (e.g., [O III], Hα; Heckman et al. 1987; Lehnert et al. 1999; Veilleux et al. 2003; Robitaille et al. 2007; Sharp & Bland-Hawthorn 2010; Rupke & Veilleux 2013; Yoshida et al. 2016; Leslie et al. 2017; McKinley et al. 2018). This work reveals that line emission extending over ~10–20 kpc distances is common around these systems. Millimeter and submillimeter interferometry has likewise been useful for tracing the spatial extent of the cold component of nearby starburst outflows (e.g., Walter et al. 2002; Bolatto et al. 2013; Geach et al. 2014; Leroy et al. 2015). Spatially resolved study of these transitions, however, has not been possible in star-forming systems beyond the very nearby universe owing to a combination of factors (including the overall weakness of the emission, difficulties differentiating emission from wind material vs. the ISM, and limited spatial resolution; Veilleux et al. 2020).

In principle, winds may also be illuminated by scattering of photons through resonant line transitions. Resonant absorption from Mg^+ and Fe^+ ions is commonly detected in absorption in galactic winds at rest-frame wavelengths $\lambda\lambda$2796, 2803 and $\lambda\lambda$2586, 2600, as these transitions are easily observable at $z > 0.2$ with blue-sensitive ground-based instruments (e.g., Rubin et al. 2010; Erb et al. 2012; Kornei et al. 2012; Bordoloi et al. 2016). Reemission of these absorbed photons (originally generated by the stellar continuum and/or line emission from

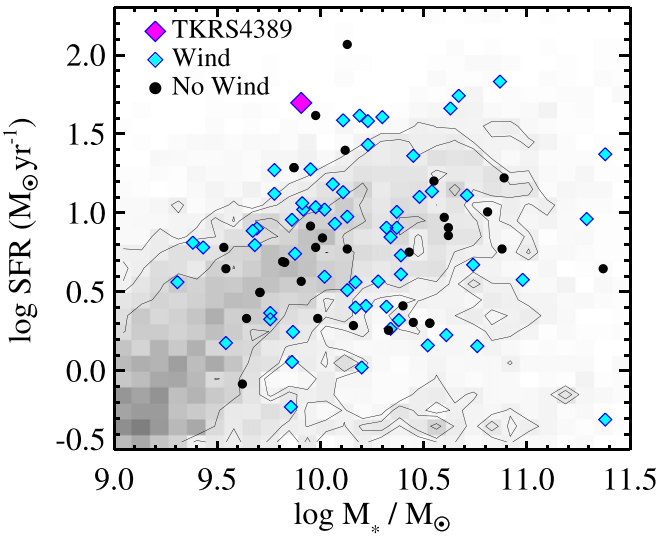

Figure 1. Gray contours show the SFR–M_* distribution of the galaxy population at $0.4 < z < 0.8$ included in the Barro et al. (2011) catalog of multiwavelength photometry for galaxies in the Extended Groth Strip. The symbols show the galaxy sample studied in Rubin et al. (2014): objects with outflows detected in Mg II or Fe II absorption are marked in cyan, and objects without detected winds are marked in black. The location of TKRS 4389 is marked with a large magenta diamond. It lies well above the star-forming sequence at $z \sim 0.7$.

H II regions; Henry et al. 2018) therefore tracks the spatial extent of the wind material. For a given shell of gas with density n, width Δr, and velocity gradient Δv, the optical depth scales as $\tau \sim n(\Delta v/\Delta r)^{-1}$ (Sobolev 1960). The surface brightness profile of the emission is a complex radiation transfer problem, modulated by gas within the ISM and by dust throughout the environment (Prochaska et al. 2011, hereafter P11; Scarlata & Panagia 2015; Carr et al. 2018). Scattering analysis then provides unique insight on the distribution and velocity of the outflow through assessment of the emergent emission profile. Moreover, the new Keck Cosmic Web Imager (KCWI; Morrissey et al. 2018), a blue-sensitive integral field unit (IFU) spectrograph on the Keck II telescope, is ideally suited to mapping these transitions. A first spectacular example was recently reported by Rupke et al. (2019), who used KCWI to trace Mg II emission to distances of ~10 kpc from a massive, compact, starbursting galaxy at $z = 0.46$. Their spectroscopic maps additionally revealed a yet brighter [O II] nebula extending to ~50 kpc from the same system.

The observations presented here targeted TKRS 4389, a $z = 0.6942$ star-forming galaxy. This system was originally identified by the Team Keck Treasury Redshift Survey (TKRS; Wirth et al. 2004), a magnitude-limited survey of the GOODS-N field (Giavalisco et al. 2004) of objects with $R_{AB} \leqslant 24.4$. It was then reobserved with Keck/LRIS as part of a survey to obtain sensitive rest-frame UV spectroscopy of galaxies having $B_{AB} < 23.0$ to measure the kinematics of cool gas traced by Mg II $\lambda\lambda$2796, 2803 absorption (Rubin et al. 2014). TKRS 4389 has a stellar mass $\log(M_*/M_\odot) = 9.9$, SFR $= 50\ M_\odot\ \mathrm{yr}^{-1}$, a morphology indicative of a merger, and indications of an active galactic nucleus (AGN; Figure 1; Rubin et al. 2010, 2014). In Rubin et al. (2010), we used the Keck/LRIS spectroscopy of TKRS 4389 mentioned above to probe the circumgalactic medium (CGM) of a close transverse foreground galaxy TKRS 4259 ($z = 0.4729$) in absorption. Analysis of the TKRS 4389

spectral features revealed P Cygni line emission in the Mg II $\lambda\lambda$2796, 2803 transitions and an outflow speed $\delta v \sim 800\,\mathrm{km\,s^{-1}}$. Indeed, this galaxy is one of only six objects of the 105 systems surveyed by Rubin et al. (2014) for which these lines are detected in emission with $>3\sigma$ statistical significance. In Rubin et al. (2011), we demonstrated that this emission is spatially extended along the slit (oriented along the galaxy's minor axis) to a distance of $\approx$7 kpc. This was the first detection of spatially extended Mg II emission from a star-forming galaxy and offered the first direct measurement of the minimum spatial extent of a wind beyond the local universe. Our constraints were nevertheless limited to the emission located along the single slit position angle, and by the relatively low signal-to-noise ratio (S/N) of the spatially resolved emission profile.

With the commissioning of KCWI, we have returned to TKRS 4389 to map the spatial extent and kinematics of this Mg II emission across the sky. In the same datacube, we may also examine line emission from resonant and nonresonant Fe II transitions, with the latter expected to be confined to the galaxy (Rubin et al. 2011; P11; but see Finley et al. 2017a). We also introduce new methodology to interpret the observations in the context of galactic wind radiative transfer models and thereby constrain properties of the phenomenon. Throughout this work, we adopt the cosmological parameters reported by Planck Collaboration et al. (2016).

2. Observations

We observed TKRS 4389 ($z = 0.6942$) in a pilot program to study the resolved emission and absorption of Mg II and Fe II of galaxies hosting known outflows originally analyzed in Rubin et al. (2014). The SFR–M_* distribution of the Rubin et al. (2014) sample is shown in Figure 1, with those objects showing outflow signatures indicated. All SFR and M_* values were obtained from SED fitting to UV, optical, and infrared broadband photometry of each target as detailed in Rubin et al. (2014). TKRS 4389 lies in the upper range of the SFR distribution of the galaxy population.

To map the spatially extended line emission originally discovered by Rubin et al. (2011), we employed the Keck Cosmic Web Imager integral field spectrograph (Morrissey et al. 2018) on the Keck II telescope. We conducted the observations on the night of 2018 January 17 UT under $\sim$1.″4 (FWHM) seeing conditions as measured at the beginning of the night.[8] Our observational setup included the M slicer, providing a $16'' \times 20''$ field of view (FOV) and sampling of $0.''70\ \mathrm{pixel}^{-1}$ (width of slices). Combined with the BL grating, this yields a spectral resolution $\mathcal{R} \sim 1800$ (FWHM). At the redshift of TKRS 4389, the FOV covers approximately 117×146 kpc along the TKRS 4389 major and minor axes, respectively. The slicer was placed so that the 0.″7-wide slices had PA = 27°, close to the PA of the galaxy's minor axis as measured from SExtractor photometry of the HST/F435W image (17°; Rubin et al. 2014). This yielded $0.''3\ \mathrm{pixel}^{-1}$ sampling along the length of each slice, with rectangular $0.''7 \times 0.''3$ pixels. Figure 2 shows the slicer orientation relative to a high-resolution, false-color image of TKRS 4389 and other galaxies in the field. Table 1 summarizes information regarding our observations.

We obtained 7×1800 s exposures on source, dithering with 1.″5 offsets between each exposure. Reduced datacubes were extracted according to standard procedures within the KCWI Data Reduction Pipeline (kderp[9]) except for the sky subtraction step (Stage 5), where we employed a custom sky subtraction algorithm optimized for this field. Stages 6–8 of the pipeline (including flux calibration) were implemented in the standard manner.

We then corrected the reduced datacubes for known astrometric errors in the WCS solution by creating white-light images for each cube, i.e., summing the flux along the spectral dimension over $\lambda = 4000$–$5500\,\mathring{A}$. The spaxel in each intensity and variance cube corresponding to the brightest pixel of its white-light image was assigned the equatorial coordinates of TKRS 4389. We then aligned the cubes by projecting each into a larger cube whose central spaxel was placed at the coordinates of TKRS 4389, adopting a simple nearest-neighbor shift for partial spaxel offsets. The WCS-corrected, aligned intensity cubes were then co-added using a weighted mean. The weights are calculated as follows: we construct a white-light image by summing all spaxels over all wavelengths except for 200 Å buffer regions on the red and blue ends, identify as "bright" pixels those with flux greater than the median flux, sum fluxes and variances in these pixels, and calculate the S/N of the summed pixels. This S/N serves as the weight for each exposure. Our fully reduced, aligned, and co-added datacube has a median (over the FOV) 1σ limiting surface brightness of 4.8×10^{-19} erg s^{-1} cm^{-2} arcsec^{-2} measured in a 5 Å wide narrowband image.

To obtain a precise estimate of the seeing and assess the extent of line emission, we employed the HST Advanced Camera for Surveys (HST/ACS) imaging from the GOODS-N field (Giavalisco et al. 2004) taken with the F435W filter. To perform a final WCS correction, we cut out the $30'' \times 30''$ portion of the ACS F435W image centered on TKRS 4389, convolved it with a small Gaussian kernel (FWHM = 0.″1), and projected the ACS image into the coordinate system of the co-added KCWI datacube using the REPROJECT[10] Python package. This yielded the model reference image/WCS. We then extracted a pseudo-broadband image from the KCWI cube using the F435W filter response function and set the reference CRPIX in the KCWI WCS to its brightest pixel and the CRVAL to the coordinates of the brightest pixel from the model reference image/WCS. Lastly, for our seeing measurement, we iteratively convolved the original F435W image with a 2D Gaussian with varying FWHM and reprojected each convolution into the *new* KCWI coordinate frame (informed by the model reference image/WCS). After reprojection, we once again set the brightest pixels to have the same coordinates (the vastly different pixel scale between ACS and KCWI induces a small offset) and output the reprojected image with its modified WCS. Least-squares minimization of the difference between this output and the co-added datacube yielded an FWHM $\sim$ 1.″63.

Herein we present several pseudo-narrowband images, which are generally produced by summing the flux over the spectral direction of the datacube between the two wavelengths indicated. With the exception of the pseudo-F435W image described above (shown in the right panel of Figure 2), we assume a flat response as a function of wavelength. A residual background gradient with flux on the order of a few percent of

[8] Note: our adopted seeing FWHM = 1.″6 as derived later in this section.

[9] https://github.com/Keck-DataReductionPipelines/KcwiDRP

[10] https://reproject.readthedocs.io/en/stable/.

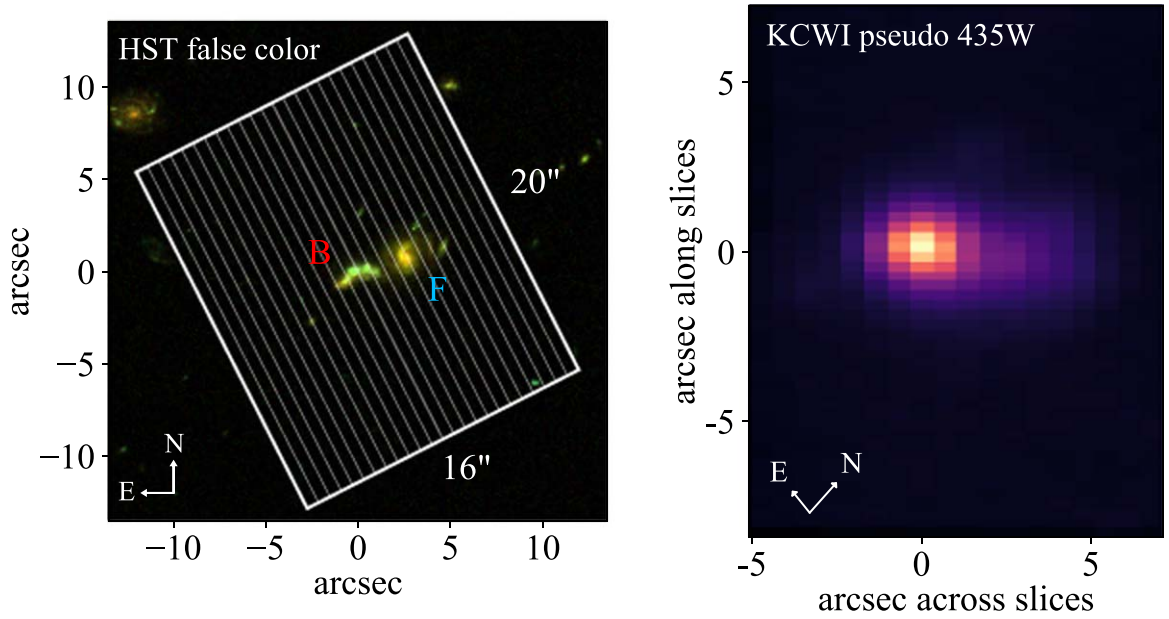

Figure 2. Left: primary KCWI slicer position and orientation superimposed on a false-color HST image composed of the ACS F435W, F606W, and F775W bands. The two brightest objects in the KCWI FOV are TKRS 4389, the focus of this paper ($z = 0.6942$; labeled "B"), and the foreground TKRS 4259 ($z = 0.4729$; labeled "F"). Right: pseudo-broadband image from the KCWI datacube FOV using the HST ACS F435W filter response function. The image has been trimmed to show only the overlapping regions from the dither pattern. Coordinates are shown relative to the brightest pixel at the center of TKRS 4389.

Table 1
Target and Observations

Target name	TKRS 4389
Coordinates (J2000)	12:36:19.84, +62:12:52.9
z	0.6942
Date of observation	17 Jan 2018 UT
Telescope/Instrument	Keck II/KCWI
Slicer/grating	Medium/BL
Exposures	7×1800s

the TKRS 4389 signal is present in these narrowband images, and we subtract this residual structure by fitting a 2D, first-degree polynomial to regions outside the detected emission from TKRS 4389.

3. Analysis

3.1. Extended Mg II Emission from TKRS 4389

From Figure 2, we find that both the HST image (left) and KCWI pseudo-435W images (right) of the TKRS 4389 field exhibit stellar continuum emission from TKRS 4389 itself ($z = 0.6942$) and a foreground galaxy TKRS 4259 ($z = 0.4729$). A subsequent publication will analyze the spatially resolved absorption profile of the foreground galaxy CGM (see Rubin et al. 2010, for an in-depth study of TKRS 4259), as we focus here on TKRS 4389. Rubin et al. (2011) showed not only that TKRS 4389 exhibits line emission and absorption from Mg II in a "P Cygni" profile cospatial with the galactic disk but also that the line emission extends beyond the regions cospatial with the stellar continuum. These prior observations, conducted via long-slit spectroscopy, were only able to measure emission along the (spatial) slit direction. With KCWI integral field spectroscopy, we obtain an array of spaxels enabling spectral analysis within each "pixel" of a 2D image.

We first search for and quantify the extent of the Mg II emission reported by Rubin et al. (2011). To remove contributions from the stellar continua of TKRS 4389 and TKRS 4259 (which overlaps with TKRS 4389 at the spatial resolution of our KCWI data), we construct a continuum-subtracted datacube wherein the spectral direction is sliced to contain a 200 Å region (4650–4850 Å) roughly centered on the observed wavelength of the Mg II doublet at the redshift of TKRS 4389. We then fitted a continuum in each spaxel over this wavelength range using a series of low-order Legendre polynomials,[11] using an iterative sigma-clipping scheme to avoid overfitting absorption or emission, and produced two versions: with the continuum subtracted and with the flux normalized by the continuum.

The left panel of Figure 3 shows a 5 Å narrowband image centered on the λ2796 emission peak and extracted from the continuum-subtracted cube. In the right three panels of Figure 3, we present spectra extracted from 24 regions containing 21 spaxels each (3×7) extending to >20 kpc above and below the disk plane (with extraction regions marked in the leftmost map). The velocity scale in each spectral panel is expressed in the reference frame of the Mg II λ2976 line. Mg II emission from both lines of the doublet is clearly detected in the large majority of these extraction regions. The physical scale labeled on the axes of Figure 3 (left) assumes our adopted cosmology and is expressed relative to the central, brightest pixel of TKRS 4389 derived from its stellar continuum image.

Figure 3 shows Mg II line emission extending well beyond the 7 kpc originally reported by Rubin et al. (2011). We now quantify the extent of Mg II emission detected by our KCWI observations. In addition to the continuum-subtracted narrow-band image described above, we sum the corresponding pixels

[11] As described in Section 2, a residual background gradient remains in the data after reduction. This continuum fitting process partially removes the ambient background signal, i.e., a small "continuum" is present in each spaxel.

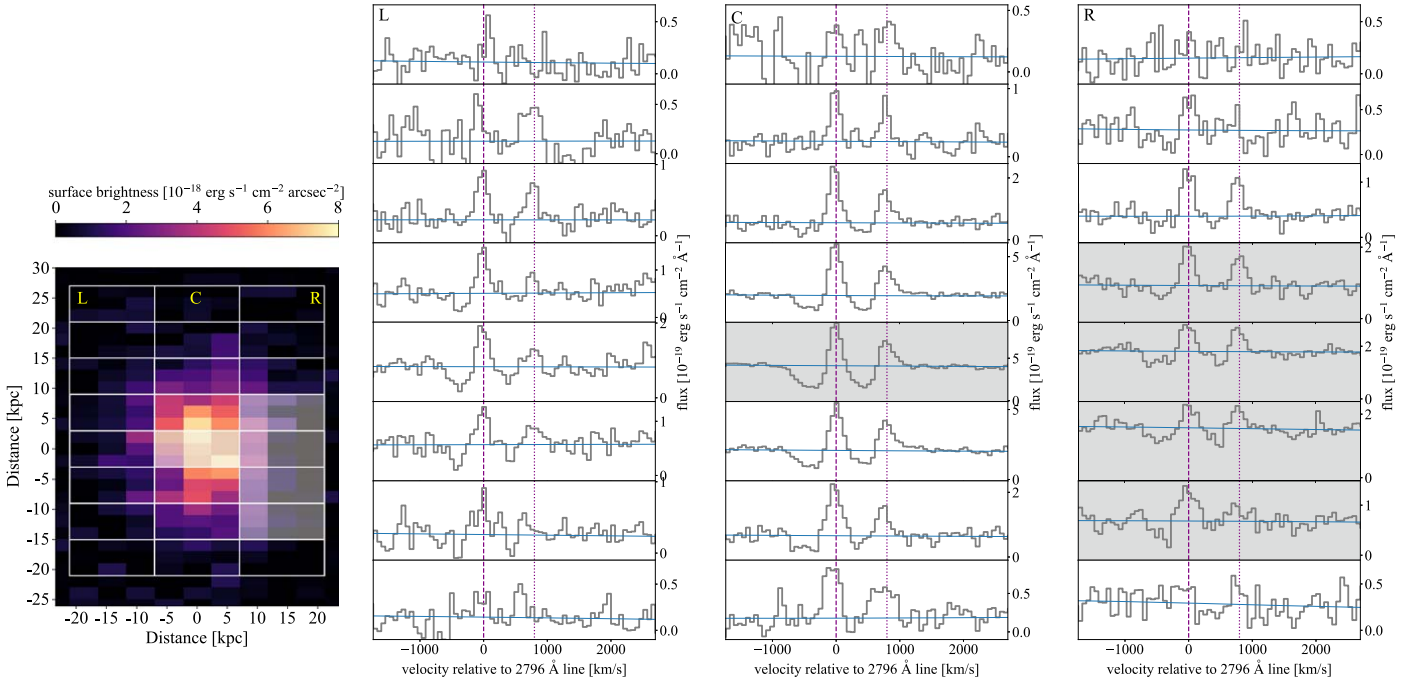

Figure 3. Mg II emission and absorption from TKRS 4389 and its CGM. The emission map on the left was constructed from a 5 Å slice (approximately 530 km s^{-1}) in the spectral direction centered on the λ2796 emission peak. Rectangles denote regions over which spaxels were co-added to produce the spectral profiles at right. Corresponding columns in the map and panels with spectra are marked "L," "C," and "R." In the three spectra panels, the vertical purple dashed line marks the reference frame set by λ2796 at the redshift of TKRS 4389 ($z = 0.6942$), and the vertical dotted line denotes the corresponding λ2803 location. Continuua fitted to the spectra using our automated algorithm are shown in blue. Spectral regions that are grayed out contain spaxels likely affected by the foreground galaxy TKRS 4259 (see Section 4.2.1), elevating the continuum level. We observe significant emission in regions distributed at nearly all azimuthal angles relative to the galaxy's minor axis, suggestive of an isotropic outflow.

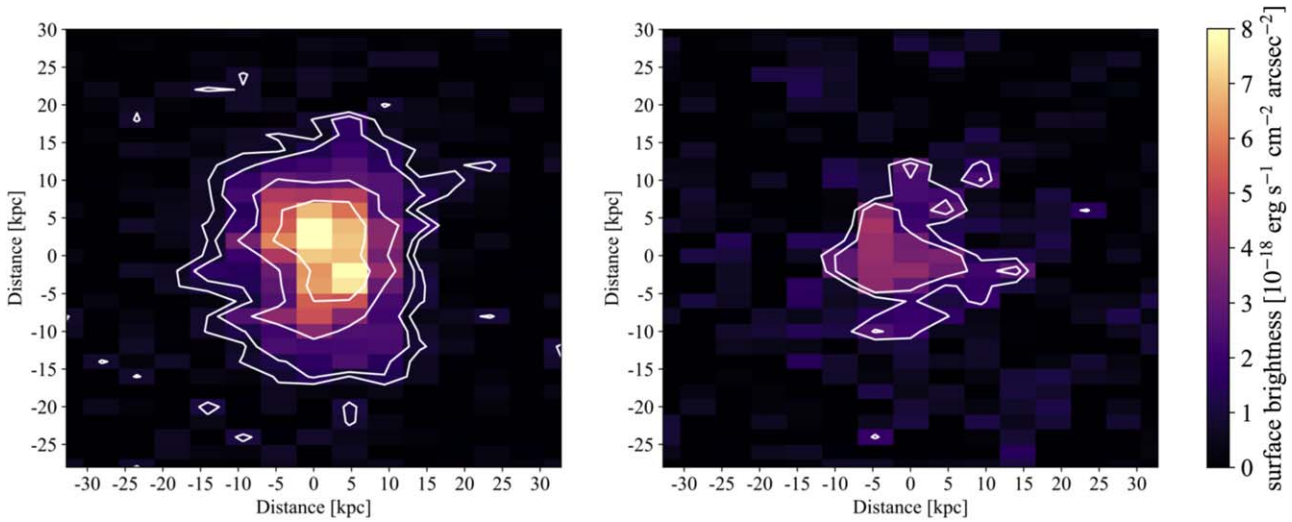

Figure 4. Surface brightness of the Mg II and Fe II* emission extracted from the continuum-subtracted KCWI datacube. Values result from summing the emission over 5 and 10 Å windows centered on the λ2796 and λ2626 emission peaks, respectively. Contours denote 2σ, 3σ, 6σ, and 10σ level detections of the emission (2σ and 3σ for Fe II*). Using 3σ as our detection threshold, the Mg II emission extends over 37 kpc in the left-hand image.

spectrally in the co-added variance cube in quadrature (over the same 5 Å window) and calculate the detection significance in each spaxel as follows:

$$S^{2796}_{j,k} = \frac{\sum_i f_{i,j,k}}{\left(\sum_i \sigma^2_{i,j,k}\right)^{1/2}} \quad (1)$$

where $S^{2796}_{j,k}$ is the significance of λ2796 emission in spaxel (j,k), $f_{i,j,k}$ and $\sigma^2_{i,j,k}$ are the flux and variance, respectively, of the ith spectral voxel in the (j,k) spaxel, and the summations run over 5 Å regions centered on the emission peak.

This calculation results in a significance map, reflected in Figure 4, with contours corresponding to 2σ, 3σ, 6σ, and 10σ detection significance. Adopting a 3σ detection threshold, we measure an extent across the significantly detected region of $5\farcs0 \pm 0\farcs4$, corresponding to 37 ± 3 kpc at the redshift of TKRS 4389. This measurement is effectively the angular separation between extreme points in the contiguous 3σ detection region, and we calculate the uncertainty as the half-

height and half-width summed in quadrature. No systematic errors related to, e.g., the WCS offset procedure described in Section 2 have been included. Below in Section 3.3, we correct for seeing by deconvolving the emission profile.

3.2. Fe II* Emission

Our KCWI cube also covers the Fe II/Fe II* $\lambda\lambda$2586, 2600, 2612, 2626, 2632 multiplet. In a similar manner to the Mg II emission, we measured the spatial distribution of continuum-subtracted emission arising from the nonresonant Fe II* λ2626 transition, chosen because it is intrinsically strongest of the Fe II* lines and is cleanly separated from the resonant Fe II transitions. Here we fitted the continuum over 4250–4550 Å, once again sigma-clipping to avoid overfitting emission/absorption. A surface brightness/significance map analogous to that of Mg II is shown in Figure 4 (right), summed over a 10 Å wavelength window centered on the λ2626 line. As shown by the contours, we only detect Fe II* emission at 3σ within approximately 7 kpc of the galaxy center (i.e., $\pm1''$). The weak but significant Fe II* 3σ emission contours in Figure 4 show potential asymmetry and offset relative to the Mg II emission, but such asymmetry and offset are essentially of the same scale as the seeing during our observations. We defer further analysis of the Fe II* emission profiles for deeper and/or higher-resolution observations.

3.3. Radial Profiles

As an additional measure of the extent of the Mg II emission, we directly compare the line emission to the stellar continuum in Figure 5. We extracted 5 Å wide pseudo-narrowband images from both the flux and variance cubes (non-continuum-subtracted) centered on (1) the λ2796 emission feature and (2) a line-free continuum region approximately 40 Å redward of the Mg II emission/absorption. We then summed the flux in 7-pixel-wide (by 1-pixel-tall) horizontal regions parallel to the major axis and extracted at successive steps along the minor axis, extending to $\sim5\farcs4$ above and below the galaxy. The variance cube was similarly summed but in quadrature. The resulting profiles from the line and continuum emission centered on TKRS 4389 are shown in the bottom panel of Figure 5 with violet and orange points/error bars, respectively. Here we have scaled the peaks of both emission profiles to one another, revealing the excess line emission extending into the circumgalactic regions, to approximately 20 kpc above and below the galaxy. The top panel plots the ratio of the two flux profiles, showing an increase in the line emission relative to the continuum moving away from the central galaxy to $\gtrsim$15 kpc toward either direction.

From our modeling in Section 2, we estimated $1\farcs6$ FWHM seeing. To control for this potentially significant effect on the measured extent of the emission, we deconvolved the emission profiles shown in Figure 5 with the seeing as follows: we fitted each with a Gaussian profile (dashed curves), subtracted in quadrature the standard deviation of a $1\farcs6$ FWHM Gaussian ($\sigma = 0\farcs68$) from the standard deviation of the fitted profiles, and produced a new Gaussian profile with this new standard deviation. The resulting deconvolved line emission profile is shown with a dotted curve in Figure 5. We estimated the Mg II emission extent without seeing effects by locating the outer points with detected emission at 5σ confidence in the original profile and the points in the deconvolved profile with those same flux values. As a result, we estimate that the emission would extend over $\sim$31 kpc without the effects of seeing.

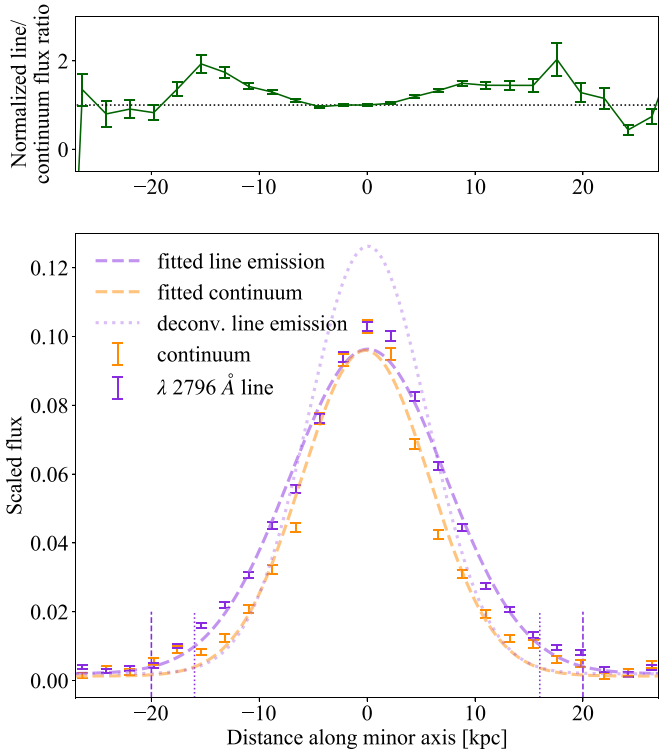

Figure 5. Bottom: flux profiles of emission from the Mg II λ2796 line (violet) and stellar continuum (orange) above and below the minor axis of TKRS 4389. The profiles have been scaled to equal amplitude at their peaks. Dashed curves represent Gaussian fits to the line and continuum data. The dotted curve shows the line profile deconvolved with the $1\farcs6$ FWHM seeing. Vertical dashed and dotted lines represent the extent of line emission detected at 5σ in both the measured and deconvolved profiles, respectively. From the deconvolved profile, we measure an extent of 31 kpc for the λ2796 Mg II emission. Top: ratio of scaled line to continuum profiles along the minor axis. Both panels show that the line emission significantly exceeds emission from the seeing-convolved stellar continuum and the seeing profile to >15 kpc both above and below the major axis. The measured line emission at ≈10–20 kpc offsets shows excess emission relative to the stellar component by factors of 30%–100%.

4. Comparison to Radiative Transfer Models

In principle, the surface brightness profile and relative velocity of the resonant Mg II emission from this galaxy depend on two distributions: (i) the spatial distribution of the source(s), and (ii) the density and velocity of Mg II ions and distribution of dust in and around the object, which absorb and scatter these photons. We may therefore constrain the latter quantities by comparing the observed emission to that predicted by models that incorporate radiative transfer effects. An implementation of Monte Carlo radiative transfer in the context of simplified galactic wind models was first described in P11. We use the same code and technique to expand on the original suite of models presented in that work, tailoring the parameter space we explore (in terms of, e.g., wind opening angle and density and velocity laws) to be suitable for our galaxy target.

4.1. Radiative Transfer Model Suite

The wind models of P11 assume a spherical continuum source with a flat spectrum (i.e., with continuum flux density

$f_\lambda \propto \lambda^0$). The radius of this source is assumed to be smaller than the inner radius of the gas composing the wind. P11 adopted a "fiducial" wind model with power-law density and velocity profiles:

$$n_{\rm H}(r) = n_{\rm H}^0 \left(\frac{r_{\rm inner}}{r}\right)^2 \quad (2)$$

$$\boldsymbol{v} = v_r(r)\hat{r} = \frac{v_0 r}{r_{\rm outer}}\hat{r}, \quad (3)$$

where $r_{\rm inner}$ is the aforementioned inner radius (set to 1 kpc), $r_{\rm outer}$ is the maximum extent of the wind (set to 20 kpc), $n_{\rm H}^0 = 0.1\,{\rm cm}^{-3}$ is the hydrogen density at $r_{\rm inner}$, and $v_0 = 1000\,{\rm km\,s}^{-1}$ is the wind velocity at $r_{\rm outer}$. The wind is assumed to have a velocity dispersion dominated by turbulent motions with a Doppler parameter $b_{\rm D} = 15\,{\rm km\,s}^{-1}$. A wind metallicity of $Z = 0.5Z_\odot$ is adopted, with dust depleting the Mg by a factor of 1/10.

As noted in P11, these choices were made in part so that the resulting model spectra would be similar in shape to Mg II profiles commonly observed in $z \sim 0.5$–1 galaxy spectroscopy (Weiner et al. 2009; Rubin et al. 2011), but they do not have special physical significance. Indeed, numerous other models are explored in P11, including those with larger values of $n_{\rm H}^0$, different density power laws (e.g., $n_{\rm H}(r) \propto r^{-3}$, r, and r^2), and different velocity profiles (e.g., $v_r(r) \propto r^{-2}$, r^{-1}, and $r^{0.5}$). The parameter space for these models is vast, and here we do not attempt a complete exploration of this space owing to the computational expense of the radiative transfer simulations and of preparing the modeled spectra for comparison to our data set (see Section 4.2).

Instead, we began by identifying model spectra from P11 that reproduce salient features of our observed Mg II profiles in a qualitative way. Isotropic models with density profiles scaling as both $\propto r^{-2}$ and $\propto r^0$ tend to yield absorption troughs with apparent optical depths that decrease with increasing velocity offsets (as observed) for several of the velocity laws explored in P11 (although this is not true in general, as can be seen in Figure 6). For simplicity, and because it is mass conserving, we chose to make use of the density scaling $n_{\rm H}(r) \propto r^{-2}$ for our model suite. We adopted a velocity law that increases linearly from $v_{\rm inner} = 50\,{\rm km\,s}^{-1}$ to $v_{\rm outer} = 500\,{\rm km\,s}^{-1}$ from $r_{\rm inner} = 1$ kpc to $r_{\rm outer}$, respectively. The velocity $v_{\rm outer} = 500\,{\rm km\,s}^{-1}$ is approximately the minimum required to reproduce the observed absorption velocities (after smoothing by the KCWI spectral resolution). Because a primary focus of our work is on constraining the spatial extent of the wind in TKRS 4389, we generated six versions of this model, changing the value of $r_{\rm outer}$ to range between 5 and 30 kpc in increments of 5 kpc. We adopt solar metallicity for the wind (in contrast to P11, who adopted $Z = 0.5Z_\odot$ as stated above) and assume that dust depletes Mg by a factor of 1/10.

Our initial comparisons of these models to the data (see Section 4.2.2) revealed that they failed to produce emission as strong as that observed at large distances from the central source. We therefore generated a supplemental set of six models with a shallower density law $n_{\rm H}(r) \propto r^{-1}$. We likewise noted that all of these models tend to yield quite broad, low-amplitude emission lines at large spatial offsets from the continuum source, whereas the emission lines observed in our datacube are narrow in velocity space (with FWHM $\approx 180\,{\rm km\,s}^{-1}$). In an attempt to simultaneously reproduce both the high velocities observed in absorption and the narrow emission features observed at distances $r \gtrsim 15$ kpc, we generated another set of 12 models, all of which have the same set of density power laws and $r_{\rm outer}$ values as above, but which have a linearly *decreasing* velocity law (with $v_{\rm inner} = 500\,{\rm km\,s}^{-1}$ and $v_{\rm outer} = 50\,{\rm km\,s}^{-1}$).

Finally, motivated by the observational evidence that such winds are often bipolar or biconical (e.g., Weiß et al. 1999; Bordoloi et al. 2011; Kornei et al. 2012; Bolatto et al. 2013; Rubin et al. 2014), we generated several models that emulate this morphology. Holding $r_{\rm outer}$ fixed at 25 kpc, for each density and velocity law described above, we modified the gas density distribution to be biconical with half-opening angles of $\phi = 10°$, 30°, 50°, 70°, and 80°. This yields an additional set of $5 \times 4 = 20$ models, for a total of 44 models when combined with those described above. Table 2 summarizes the parameters of all the models we generated.

Model spectra are calculated using the 3D Monte Carlo radiation transfer code of Kasen et al. (2006) as described in detail in P11. Briefly, the values of the wind density and velocity are mapped onto a 3D Cartesian grid with a pixel size of 0.2 kpc. Each simulation follows the paths of $N \sim 10^7$ photon packets as they are absorbed and reemitted throughout the grid until they exit the grid region. All photons with wavelengths between 2770 and 2830 Å are included in the output and are binned to a dispersion of 0.25 Å. The images and spectra of each model shown correspond to a viewing angle $\theta = 90°$, although we generated and inspected models with a wide range of viewing angles. This choice is unimportant for our analysis of the isotropic wind models; however, changes in viewing angle can produce qualitatively different output spectra for biconical winds. For example, all such models produce little to no absorption when viewed at $\theta = 90°$, whereas if the outflow cones were tilted such that more of the wind material were aligned with our line of sight to the continuum source, they would produce progressively stronger absorption (e.g., Carr et al. 2018). We will explore these nuances in future analyses. Most importantly, the biconical models with $\theta < 90°$ are qualitatively inconsistent with our data owing to excess emission offsets redward and blueward of the systemic velocity in spectra extracted above and below the galaxy disk. As shown in Figure 3, the Mg II emission essentially peaks at the systemic velocity of TKRS 4389 in spectra extracted in all directions from the center of the galaxy.

Figure 6 displays spectra and surface brightnesses predicted for a subset of these models with $r_{\rm outer} = 25$ kpc. Total surface brightness maps, along with maps showing the surface brightness predicted for two $100\,{\rm km\,s}^{-1}$ wide wavelength windows, are shown. The primary effect of varying the wind density profile between $n_{\rm H} \propto r^{-2}$ and r^{-1} is to boost the surface brightness in the wind outskirts for the latter models (shown in the second, fourth, and fifth rows). As seen by comparing the rightmost panels of Figure 6, winds that decline in velocity with radius produce much weaker emission in the wind outskirts at wavelengths corresponding to relative velocities $\delta v > 200\,{\rm km\,s}^{-1}$.

4.2. Direct Comparison to KCWI Spectroscopy

The outflow geometry, densities, velocities, etc., dictate both the projected surface brightness profile of line emission and the

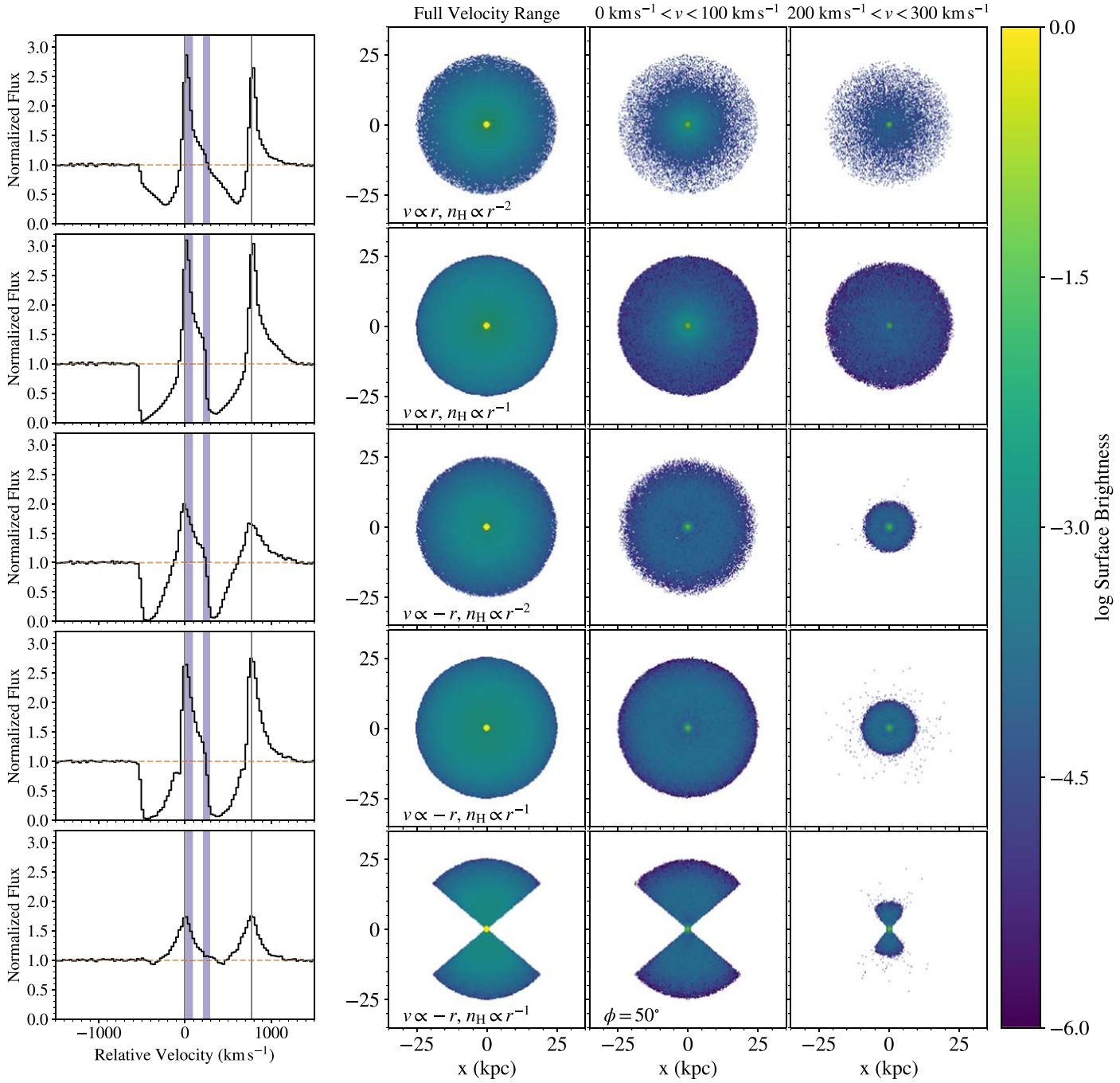

Figure 6. The top four rows show spectra and surface brightness profiles predicted for isotropic wind models with the four combinations of velocity and density laws described in Section 4.1. The bottom row shows these same properties for a biconical wind model having a half-opening angle $\phi = 50°$ and with a decreasing velocity law ($v(r) \propto -r$) and a density power law $n_H(r) \propto r^{-1}$. The spectra shown at left include all photons within the computational domain at wavelengths corresponding to velocities -1500 km s^{-1} $< \delta v <$ 1500 km s^{-1} relative to the λ2796.35 transition. The vertical blue bars indicate the limits of the velocity ranges shown in the images to the right (as labeled on top). The vertical gray lines mark the rest velocities of the two doublet transitions.

spectral profiles observed across the system. Therefore, to achieve the most direct comparison between the radiative transfer models described above and our KCWI data, we compare both the spatial and spectral dimensions simultaneously. Among several key differences between the raw model and KCWI cubes, the model outputs have much higher spatial and spectral resolution than the data, even without considering the effects of seeing. Below, we detail how we prepared the models for comparison, as well as the results that followed from this comparison.

4.2.1. Procedure

A number of operations are required to manipulate the datacube products of our radiative transfer model software so that they may be effectively compared to the KCWI datacube. First, we convolve the "image" predicted within each 0.25 Å wide wavelength bin with a 2D Gaussian kernel with FWHM $= 1\farcs63$ (as derived from HST imaging; see Section 2) to emulate the effects of seeing. We then rebin each image channel to the spatial pixel scale of our KCWI data, approximately $0\farcs68 \times 0\farcs29$ measured from the WCS in the

Table 2
Radiative Transfer Model Parameters

Parameter	Values
ϕ	10°[a], 30°[a], 50°[a], 70°[a], 80°[a], 85°, 86°, 87°, 88°, 89°, 90°[a]
$r_{\rm outer}$	5, 10, 15, 20, 25[a], 30 kpc
$n_{\rm H} \propto$	r^{-1}[a], r^{-2}[a]
$v \propto$	$-r$[a], r[a]
θ	20°, 40°, 60°, 80°, 90°[a]
$r_{\rm inner}$	1[a] kpc
$v_{\rm inner}$	50[a], 500[a] km s^{-1}
$v_{\rm outer}$	50[a], 500[a] km s^{-1}

Note.
[a] Included in the left panel of Figure 7.

KCWI data. The models are expressed in physical distance coordinates (kpc), so we convert to angular distances assuming our adopted cosmology (Planck Collaboration et al. 2016). We then add a World Coordinate System (WCS) solution onto the model datacubes with the appropriate KCWI spatial pixel scales. The reference pixel coordinates were determined by locating the brightest pixel in a 75 Å wide (4700–4775 Å) pseudo-narrowband image constructed from the model cube and setting the coordinates of that pixel to the coordinates of the brightest pixel in a similar pseudo-narrowband image of the observed data.

At this point, the spectral dimension of the transformed model cubes remains mismatched to the KCWI data and is expressed in the rest frame. We thus redshift the full wavelength scale to that of TKRS 4389. Then, for each spaxel, we convolve the spectrum with a Gaussian line-spread function concordant with the spectral resolution documented for the BL grating/medium slicer combination ($\mathcal{R} \sim 1800$). As a final step, we rebin each spaxel to the same dispersion as the KCWI data (1 Å pixel^{-1}).

With the spatially and spectrally convolved and rebinned model cubes now aligned with the KCWI data, we directly compared the models to the data on a spaxel-by-spaxel basis. For both the model and KCWI cubes, we extracted spectra in 2-spaxel, $0\farcs7 \times 0\farcs6$ apertures (1 horizontal spaxel and 2 vertical spaxels). Then, to compare the two, we found scaling factors between the continua in extracted spectra from the models and from the data, where continuum regions were defined as pixels where 4700 Å $< \lambda <$ 4720 Å, which contain neither absorption nor emission features. We adopted the ratio of the median continuum flux value in the data to that of the model, omitting pixels with negligible continuum flux, as each extracted spectrum's scaling factor. We then adopted as each model's global scaling factor (over the entire FOV) the median scaling factor of the extracted spectra.

However, a portion of the KCWI FOV is "contaminated" by the foreground galaxy TKRS 4259 (Rubin et al. 2010), which increases the continuum level relative to the line emission in affected pixels. Fortunately, TKRS 4259 is primarily situated to the west–northwest of TKRS 4389, and its light overlaps only slightly with the stellar disk of TKRS 4389 at the spatial resolution of our data, leaving most of the projected area around TKRS 4389 unaffected. Nevertheless, we identified spaxels potentially contaminated by TKRS 4259 by assuming that its stellar continuum will contaminate the same spaxels that also contain [O II] line emission at the redshift of TKRS 4259 ($z = 0.4729$), which we also cover with these KCWI observations. We omitted these spaxels from both the continuum scaling determination and the model–data comparison, as indicated in Figure 3, where regions with contaminated spaxels are grayed out (although uncontaminated spaxels within each region were still used in the fits). Lastly, we are primarily concerned with the Mg II emission arising from the galactic wind, and Mg II emission is likely also produced in galactic H II regions. Rubin et al. (2011) reported strong emission from H II region signatures such as [O II], Hγ, and Hδ in the central regions of TKRS 4389. Therefore, we omitted 3 spaxels within $\sim 0\farcs4$ of TKRS 4389, centered on the brightest continuum spaxel, from the comparison.

Finally, we adopted an rms of residual values as our goodness-of-fit metric for each model i:

$$\mathrm{rms}_i = \sqrt{\frac{\sum_{j,k}(\mathcal{D}_{jk} - (s_i \mathcal{M}_{ijk}))^2}{N}}, \quad (4)$$

where $\mathcal{D}$ and $\mathcal{M}$ denote the KCWI data and radiative transfer models, respectively, i and j subscripts denote individual model cubes and individual extracted spectra from each cube (model or data), respectively, k subscripts denote individual pixels in each spectrum, s_i is the scaling factor for each model cube found as described above, and N represents the total number of extracted spectra j included in the comparison. The rms is calculated over the 75 Å spectral region from 4700 to 4775 Å, covering the observed wavelength regions containing the Mg II doublet and ~25 Å continuum regions on either side. Spatially, we include spaxels over an area approximately 60×70 kpc centered on the brightest continuum spaxel of TKRS 4389, omitting those labeled as contaminated.

4.2.2. Results

A number of results emerge from our model comparison, summarized in Figure 7. A subset of our convolved models are plotted in Figure 8. The left panel of Figure 7 depicts the residual rms values for each of our models with a black circle, with the circle sizes representing the $r_{\rm outer}$ extent values (larger circles for greater $r_{\rm outer}$). Particular density ($n \propto r^{-1}$) and velocity ($v \propto -r$) profile shapes are shown with diagonal hatching and green diamonds, respectively. Histograms of the rms values are shown in the middle panel with density/velocity profiles similarly marked, with declining velocities colored green. The right panel shows only the isotropic models, with rms as a function of wind radial extent. For reference of our goodness-of-fit metric, the models plotted in green, orange, and purple in Figure 8 have rms = 9.5, 8.7, and 8.6, respectively.

Most prominently, isotropic models are strongly favored over those with smaller $\phi \leqslant 80°$; the best fitting is colored purple in Figure 8. Indeed, collimated outflow geometries with $\phi = 10°$ universally show the largest rms relative to the full rms distribution, i.e., changing the extent and velocity or density profiles did not improve the fit because these models produced insufficient flux away from the minor axis. The isotropic models ($\phi = 90°$) attain the smallest residuals of any opening angle, and, indeed, the rms trends downward with increasing opening angle. For clarity, we do not include intermediate ϕ values between 80° and isotropic in Figure 7. However, we also generated and compared models with intermediate ϕ values of 85°–89°; their resulting rms values indeed progressively and sharply converge downward toward those of the isotropic

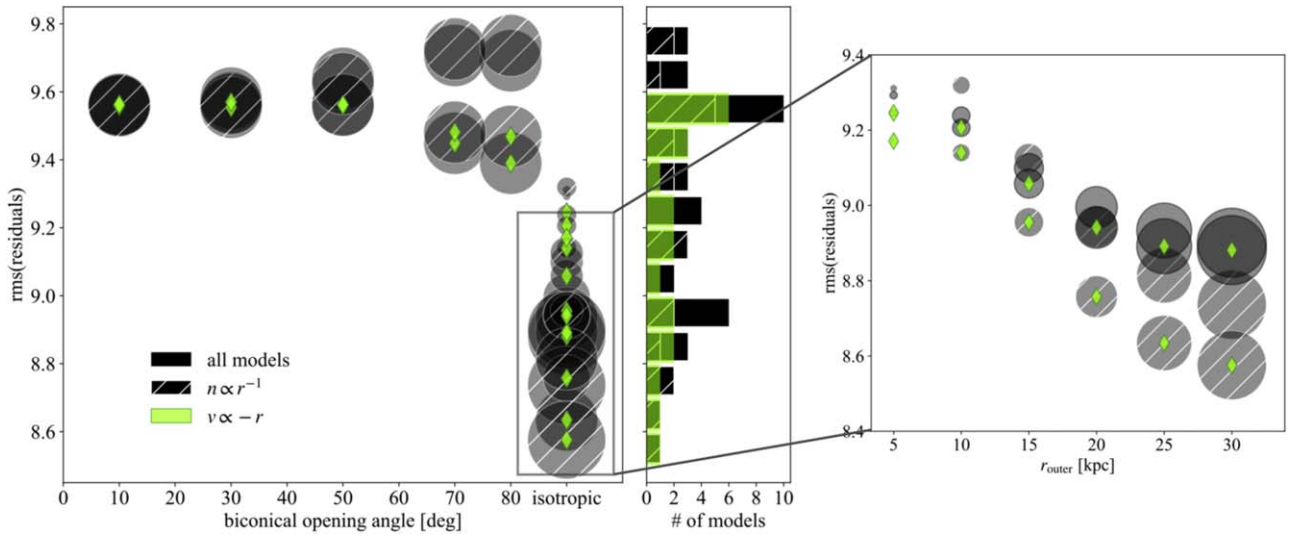

Figure 7. Goodness of fit for our 3D radiative transfer models given various choices of wind properties. Left: all model rms values are shown as a function of wind opening angle ϕ in black circles sized according to r_{outer} (and black histograms in the middle panel). Note that we only include $r_{outer} = 25$ kpc models for those with $\phi < 90°$. Certain model parameter choices are highlighted, such as those with $n \propto r^{-1}$ density profiles rather than $n \propto r^{-2}$, and those with radially decreasing rather than increasing velocity profiles. Right: showing only the isotropic wind models ($\phi = 90°$), we demonstrate the impact of wind extent (r_{outer}), density profile, and velocity profile. The best-fitting models are winds with isotropic geometries, $r_{outer} > 20$ kpc, $n \propto r^{-1}$, and radially declining velocity profiles.

geometry. We acknowledge that some substructure in the Mg II emission maps of Figures 3 and 4 may be apparent to some readers. However, we note that key pixels that would contribute to such apparent substructure have been omitted from our modeling (see Section 4.2.1). We therefore conclude that, given KCWI's resolution and the contamination from TKRS 4259, we lack substantial quantitative evidence for such substructure that might invalidate our finding that the isotropic models indeed best fit the observations.

Second, the modeling provides an additional constraint on the outflow extent to that measured directly in Section 3.1. The right panel of Figure 7 shows only the isotropic models and demonstrates that the models with the smallest rms values have $r_{outer} > 20$ kpc. Those with $r_{outer} \leqslant 10$ kpc have insufficient flux at large radii from the galaxy and consistently perform more poorly (regardless of changes in density/velocity profile) with rms greater than the $r_{outer} > 20$ kpc isotropic models. Although this result is unsurprising given the results of Section 3.1, this consistency suggests that the extended signal we observe is not the spurious result of, e.g., poorly understood instrumental blurring effects.

Lastly, the models that best fit our data feature *radially declining* velocity profiles (green diamonds in Figure 7), with initial velocities $v_{inner} = 500\,km\,s^{-1}$ and final velocities $v_{outer} = 50\,km\,s^{-1}$. The impact of the wind velocity is most evident in the Mg II emission profiles at large radii, which we demonstrate in Figure 8, where we superimpose both data and model extractions from regions illustrated in Figure 3. In particular, a wind with radially increasing velocity broadens the emission profile, and the modeled profile exhibits excess flux at velocities offset from the systemic and insufficient flux at the systemic velocity.

5. Discussion

5.1. Origin of the Outflow

Rubin et al. (2010) and Rubin et al. (2014) report that TKRS 4389 exhibits some level of AGN activity, has SFR $\sim 50\,M_{\odot}\,yr^{-1}$, and is undergoing a merger, all phenomena that likely eject gas from galaxies. As described in Section 4, our data suggest an outflow that is close to isotropic and strongly disfavor biconical models that are highly collimated. One may intuitively expect AGN-driven outflows to be relatively collimated owing to the minuscule physical scale of a black hole accretion disk relative to its host galaxy and the presence of collimated jets observed at X-ray, optical, and radio wavelengths in some nearby active galaxies. However, any resulting outflows from AGN-driven jets will depend on the energy output of the AGN and the coupling of this energy to the surrounding ISM. If the coupling is strong, the outflow should follow the pressure gradient of the medium (Veilleux et al. 2020, and references therein). On the other hand, galaxy-wide star formation episodes naturally provide the spatially distributed matter and energy injection to drive less collimated outflows via, e.g., supernovae, radiation pressure, and cosmic rays (e.g., Murray et al. 2010, 2011; Thompson et al. 2015). However, observations of galaxies hosting active nuclei indicate that AGNs can indeed drive galaxy-scale outflows (Harrison et al. 2012; Leung et al. 2017).[12] Baron et al. (2018) mapped with KCWI an outflow traced by [O III] emission from a post-starburst galaxy with an active black hole. Their map reveals a 17 kpc asymmetric conical structure only present to one side of the galaxy, far different from the symmetric wind we observe around TKRS 4389, and stellar population and dynamical modeling indicate an AGN-driven outflow. Rupke & Veilleux (2015) likewise mapped the inner < 3 kpc of a nearby ULIRG hosting a quasar-driving wind with the IFU mode of the Gemini Multi-Object Spectrograph (South), tracing the outflow across the FOV in both Na I absorption and resonantly scattered emission. Although geometry alone will likely not discriminate between outflow mechanisms, the emerging diversity of wind geometries from spatially resolved observations will serve as important constraints for both small-scale (Fielding et al. 2017) and large-scale (Nelson et al. 2019) modeling of galactic winds.

[12] However, we qualify that TKRS 4389 is very different from these AGN-selected samples, e.g., with an X-ray luminosity $\geqslant 2$ orders of magnitude fainter (Ptak et al. 2007).

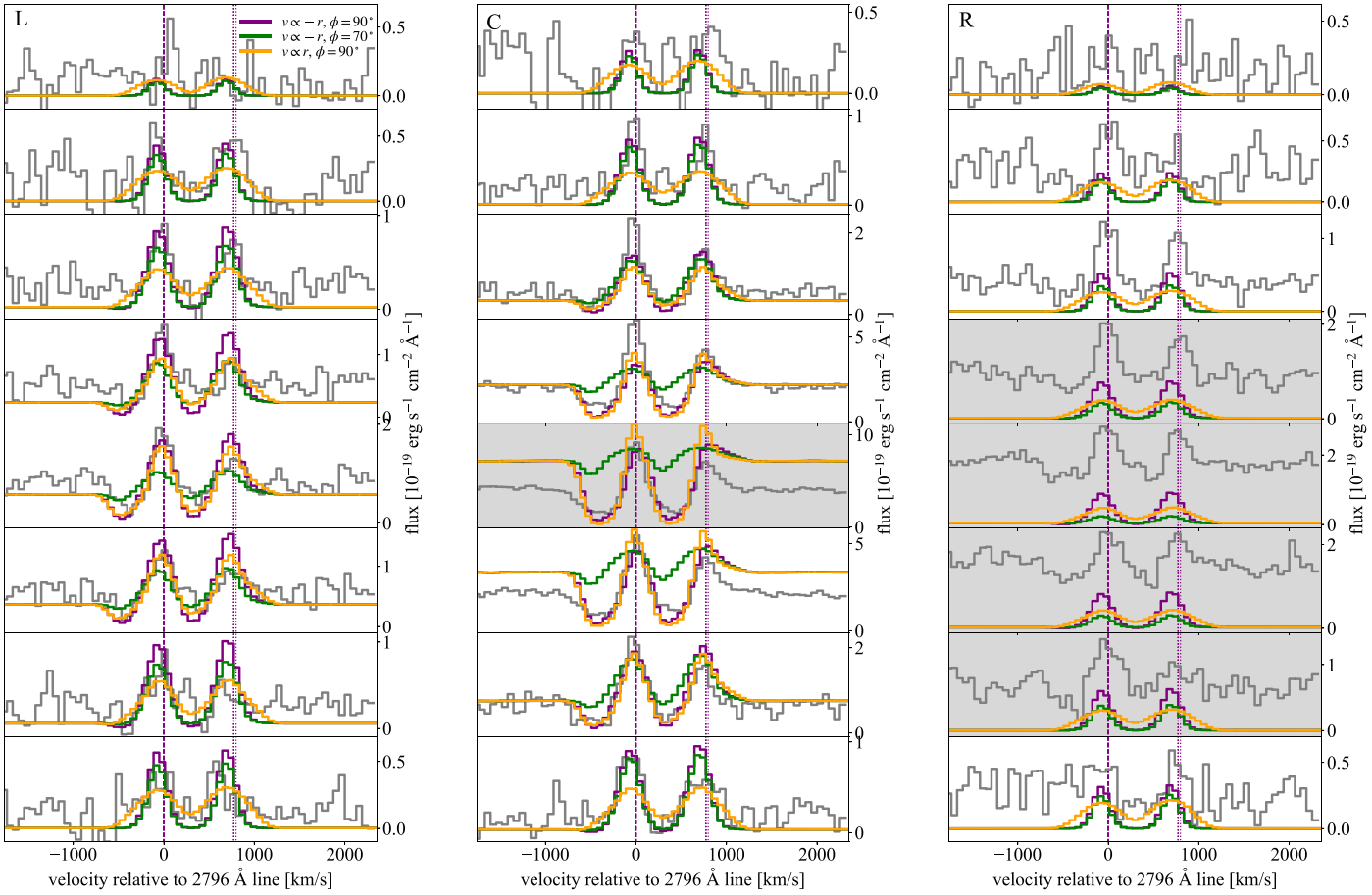

Figure 8. Comparison of spectra extracted from our KCWI data with those extracted from our 3D radiative transfer models. Each column of panels corresponds to a column depicted in Figure 3 (left) with the same "L," "C," or "R" label. Within each panel, we plot three extractions from three models, all of which have $n \propto r^{-1}$ density profiles: the best-fit model, which is isotropic and has a radially declining velocity profile and $r_{\rm outer} = 25$ kpc (purple); a more collimated wind, also radially declining in velocity and with $r_{\rm outer} = 25$ kpc but with $\phi = 70°$ (green); and an accelerating, isotropic wind with $r_{\rm outer} = 30$ kpc (orange). This final model is indeed the second-best fitting, and we note that this model poorly matches the data in both the width and height of the emission peaks, especially at large radii. As in Figure 3, panels containing spaxels omitted from the model fits according to Section 4.2.1 have gray backgrounds.

The irregular morphology and high SFR of TKRS 4389 suggest that it may share some physical similarities with the class of ultraluminous IR-bright systems (ULIRGs) undergoing concurrent mergers and starbursts at low redshift (Sanders & Mirabel 1996). UV to IR MAGPHYS SED fitting to the broadband photometry of this object (described in Rubin et al. 2014) yielded a best-fit value for the total dust luminosity $L_{\rm dust} \approx 4.4 \times 10^{11}\, L_{\odot}$, i.e., below the $L_{\rm IR} > 10^{12} L_{\odot}$ threshold defining ULIRGs (Sanders & Mirabel 1996). This, in combination with the blue colors of our target, makes it an imperfect analog of dust-dominated ULIRGs; however, they may nevertheless have similarities in their wind geometries and driving mechanisms. The significant observational evidence for the ubiquity of winds traced both in Na I D and OH absorption and in CO emission in these systems (e.g., Rupke et al. 2005a; Martin 2005; Rupke & Veilleux 2013; Veilleux et al. 2013; Cicone et al. 2014; Lutz et al. 2020) strongly suggests that they likewise have an isotropic geometry (as argued by, e.g., Lutz et al. 2020). The relative importance of star formation versus AGN activity in driving ULIRG winds remains to be firmly established; however, a scenario in which star formation plays an important role in launching winds wherever it is present, with AGN contributing a "boost" in mass outflow rates that is correlated with AGN luminosity, has emerged in recent years (Veilleux et al. 2013; Cicone et al. 2014; Fiore et al. 2017; Lutz et al. 2020).

Nelson et al. (2019) track outflows driven by both supernovae and AGN feedback in the Illustris TNG50 simulation and find that while both supernova and AGN-driven winds may begin with large, near-isotropic opening angles near the galaxy, the outflows become collimated on larger scales as the wind travels through the CGM. This effect intensifies at lower redshift in their simulations and is prominent by $z \sim 1$; however, the simulated winds are nearly isotropic on the scales we observe here ($\sim$20 kpc) and become more collimated at the scales typically probed in QSO absorption-line experiments (Bordoloi et al. 2011; Kacprzak et al. 2012).

5.2. Mg II Emission Mechanisms

In our analysis, we have made the assumption that the observed Mg II emission has arisen purely as a result of resonant scattering of photons through the cool photoionized outflow driven by the target galaxy. However, there are at least two other potential mechanisms that may give rise to Mg II emission from diffuse circumgalactic material: recombination of Mg^{++} ions, and collisional excitation of the Mg II $\lambda\lambda$2796, 2803 doublet transitions. Indeed, collisional excitation is

predicted to yield significant emission in other rest-frame UV metal-line transitions tracing the CGM, e.g., C III λ977 and Si III λ1207 (van de Voort & Schaye 2013; Sravan et al. 2016; Corlies et al. 2020). We therefore assess here the potential contributions of these processes to the observed emission using the spectral synthesis code CLOUDY (version 17.01; Ferland et al. 2017).

We consider a simplified scenario of an optically thin, infinite slab of gas having solar metallicity and three different hydrogen volume densities: $n_{\rm H} = 0.1$, 0.01, and 0.001 cm^{-3}. For our source of ionizing photons, we adopt the extragalactic UV background provided to Ferland et al. (2017) by Haardt & Madau[13] and interpolated to $z = 0.7$. For this set of conditions, CLOUDY predicts ionization parameters ranging between $\log U = -2.1$ and -4.1 for the lowest and highest volume densities, respectively, and neutral hydrogen fractions in the range $x_{\rm HI} \approx 10^{-4}$–$10^{-1}$. The resulting slabs range in thickness ($d\ell = N_{\rm HI}/x_{\rm HI} n_{\rm H}$) from $\approx$4 kpc to $\approx$0.4 pc, and the predicted Mg II doublet emissivities range between 10^{-32} and 10^{-27} erg cm^{-3} s^{-1}. Assuming that these emissivities arise from a 1 kpc^3 cube of gas at $z = 0.7$, the resulting Mg II λ2796 surface brightness would be 7.6×10^{-23} erg s^{-1} cm^{-2} arcsec^{-2} for $n_{\rm H} = 0.001$ cm^{-3}, 1.4×10^{-20} erg s^{-1} cm^{-2} arcsec^{-2} for $n_{\rm H} = 0.01$ cm^{-3}, and 8.7×10^{-19} erg s^{-1} cm^{-2} arcsec^{-2} for $n_{\rm H} = 0.1$ cm^{-3}. The predicted Mg II λ2803 surface brightnesses are $\approx$30%–50% lower. The former two values are well below the surface brightness detection limit of our observations (1.4×10^{-18} erg s^{-1} cm^{-2} arcsec^{-2} at 3σ), and all are well below the surface brightness of the extended emission we observe at $>2 \times 10^{-18}$ erg s^{-1} cm^{-2} arcsec^{-2}.

We caution that the assumption of a 1 kpc thick cloud is technically inconsistent with our assumption of optically thin conditions, as such a cloud would likely give rise to optically thick H I at densities $n_{\rm H} \sim 0.01$–0.1 cm^{-3} (e.g., Rahmati et al. 2013). A more physically plausible scenario would be one in which there are numerous, small, dense clouds filling a larger-scale hot flow (e.g., Rauch et al. 1999; Crighton et al. 2013, 2015; Lau et al. 2016; McCourt et al. 2018; Gronke & Oh 2018). The surface brightnesses reported above may be considered the maximum values that would arise from this type of cloud geometry.

5.3. The Mass of the Flow

In "down-the-barrel" absorption-line studies of outflows, estimates of mass outflow rates are typically approached as follows (Rupke et al. 2005b; Weiner et al. 2009; Martin et al. 2012; Rubin et al. 2014). First, a fiducial flow morphology is adopted; often, this is an axisymmetric bicone extending to a distance $r_{\rm outer}$ from each galaxy's center. The gas is assumed to remain at a constant velocity v_0 as it flows outward. The resulting mass outflow rate may be written as

$$dM/dt = \frac{4\pi}{3} C_\Omega \mu m_p N_{\rm H,flow} r_{\rm outer} v_0, \quad (5)$$

with C_Ω equal to the angular covering fraction of the bicone and μm_p equal to the mean molecular weight. $N_{\rm H,flow}$ is the total hydrogen column density along a line of sight through the bicone and is to some extent constrained by the data via analysis of blueshifted metal-line absorption in transitions such as Mg II, Fe II, or Na I. However, ionization fractions, metal abundance ratios, and dust depletion factors must be adopted in order to estimate $N_{\rm H,flow}$ from metal-line column densities, all of which are poorly constrained and uncertain by orders of magnitude. The velocity, v_0, is the most tightly constrained quantity in this context, as it may be measured directly from the galaxy spectroscopy. The extent of the flow, $r_{\rm outer}$, and the morphology of the putative bicone are typically constrained by these data only in the sense that the material must extend over a considerable area of the luminous component of the galaxy in order to give rise to any detectable absorption (and so, e.g., likely extends to at least the half-light radius with an angular covering of $C_\Omega \gtrsim 1/2$; Weiner et al. 2009; P11).

The emission-line data and analysis presented above eliminate several of the major sources of uncertainty in estimates of the mass flow rate. First, our analysis directly constrains the morphology and extent of the wind, suggesting that it is isotropic (such that $C_\Omega = 1$) and extends to at least $r_{\rm outer} \geqslant 20$ kpc. For this particular galaxy with a half-light radius $R_e = 3.8$ kpc (Rubin et al. 2014), using the latter values ($r_{\rm outer} = 20$ kpc and $C_\Omega = 1$) in the above equation increases dM/dt by a factor of $\sim$10. Adopting the Fe II column density measured for the wind in this system by Rubin et al. (2014) of $\log N_{\rm FeII,flow}/{\rm cm}^{-2} > 14.8$, and assuming that all Fe is singly ionized, a solar abundance ratio (logFe/H $= -4.49$; Savage & Sembach 1996), and a dust depletion factor of -1.0 dex (as in Rubin et al. 2014), we find that $\log N_{\rm H,flow}/{\rm cm}^{-2} > 20.3$.[14] Under the assumption of a spherically symmetric wind extending to $r_{\rm outer} = 20$ kpc with $v_0 = -300$ km s^{-1} (and $\mu = 1.4$), we estimate $dM/dt \approx 57\, M_\odot$ yr^{-1}—a value comparable to the SFR of this system.

The simple wind morphology adopted for this estimate, however, is inconsistent with the geometry of the 3D wind model favored by our data set. Instead of a wind with a constant density and velocity, the observed Mg II profile is most closely matched by a wind with a velocity and density that decline as a function of distance. In particular, the model yielding the smallest rms value as described in Section 4.2.2 has velocity and density laws:

$$v(r) = -18.75 \text{ km s}^{-1} \text{ kpc}^{-1}(r - r_{\rm inner}) + v_{\rm inner}$$
$$n_{\rm H}(r) = 0.1 \text{ cm}^{-3}(r_{\rm inner}/r),$$

with $r_{\rm inner} = 1$ kpc and $v_{\rm inner} = 500$ km s^{-1} (assuming a solar abundance ratio for Mg, that all Mg is Mg$^+$, and a dust depletion factor of -1.0 dex). Given these profiles, we may calculate the mass flow rate as a function of r:

$$\frac{dM}{dt}(r) = 4\pi \mu m_p n_{\rm H} r^2 v,$$

or

$$\frac{dM}{dt}(r) \approx 22\, M_\odot {\rm yr}^{-1} \frac{r}{1 \text{ kpc}} \frac{v(r)}{500 \text{ km s}^{-1}}.$$

Due to this diverging density law, the mass flow rate rises from 22 $M_\odot$ yr^{-1} at the base of the wind ($r = 1$ kpc) to $\sim$147 $M_\odot$ yr^{-1}

[13] This radiation field was provided to Ferland et al. (2017) in a private communication by F. Haardt in 2005 and is a modification of the UV background radiation field published in Haardt & Madau (1996).

[14] We choose to make use of our constraints on $N_{\rm FeII,flow}$ rather than $N_{\rm MgII,flow}$ because the absorption-line analysis performed in our earlier work did not explicitly model the effects of scattering, which are far more significant in the latter case.

at $r = 10$ kpc, with $v(r = 10\,\mathrm{kpc}) \approx 330\,\mathrm{km\,s^{-1}}$. The flow rate decreases at larger radii, to $\sim 55\,M_\odot\,\mathrm{yr}^{-1}$ at $r = 25$ kpc. The analogous model with an increasing velocity law yields $\frac{dM}{dt}(r = 1\,\mathrm{kpc}) \approx 2.2\,M_\odot\,\mathrm{yr}^{-1}$ and $\frac{dM}{dt}(r = 10\,\mathrm{kpc}) \approx 97\,M_\odot\,\mathrm{yr}^{-1}$.

For context, the halo mass for this system, estimated using the stellar-to-halo mass relation of Moster et al. (2013) for the stellar mass $\log M_*/M_\odot = 9.9$ at $z = 0.69$, is $\log M_h/M_\odot \approx 11.7$. Such a halo has a virial radius $R_{\mathrm{vir}} \approx 143$ kpc (assuming that it collapsed at the epoch of observation as is conventional; Maller & Bullock 2004). Studies of outflows in cosmological zoom simulations such as the FIRE suite (Muratov et al. 2015, 2017) have focused on measuring flow rates at distances $\geqslant 0.25R_{\mathrm{vir}}$, which for this system is beyond the extent of any of our adopted wind models ($0.25R_{\mathrm{vir}} \approx 36$ kpc). They assess the average cumulative mass-loading factor $\eta = \frac{dM/dt}{\mathrm{SFR}}$ as a function of halo mass and redshift, finding that values of η tend to fall in the range $1 < \eta < 10$ for halo masses $M_h \sim 10^{11.7}\,M_\odot$ at $0.5 < z < 2$. This range is consistent with the mass flow rate and resulting value of $\eta \sim 1$ we estimate for distances of $r = 25$ kpc above.

Given our best-fitting wind velocity radial profile, the outflowing wind material is unlikely to escape the gravitational potential of the galaxy, despite the vigorous episode of star formation TKRS 4389 is undergoing. Assuming an $M_h \sim 10^{11.7}\,M_\odot$ halo with a Navarro–Frenk–White profile and the halo concentration parameters from Ragagnin et al. (2019), we estimate an escape velocity of $195\,\mathrm{km\,s^{-1}}$ at 25 kpc. Thus, the velocity implied by our wind model ($50\,\mathrm{km\,s^{-1}}$) falls well short of the escape speed. Instead, the material is likely to fall back onto the galaxy in a "galactic fountain" (e.g., Fraternali & Binney 2006; Armillotta et al. 2016). We add the caveat that our third-best fitting model, with a radially increasing velocity profile, would in fact exceed the escape velocity at this radius.

More broadly, the wide range in the estimates of mass outflow rate listed above illustrates the importance of wind morphologies and velocity profiles in determining the impact of these flows on their host galaxies. It also implies that a more general and complete exploration of the parameter space of wind density distributions and velocity laws—if this were to yield a different "best-fit" wind morphology—could result in significantly different mass outflow rates. Here we simply report our best estimates of the mass flow rate under the assumption of the adopted density and velocity laws, the combination of which successfully reproduces the detailed features of the observed Mg II profiles. Regarding the physical origin of our observed wind, our best-fit model suggests a scenario in which either the wind sweeps along material encountered as it leaves the galaxy or the cool wind mass increases owing to in situ condensation (e.g., Thompson et al. 2016), as the $n \propto r^{-1}$ profile requires that mass is added as distance increases. Profiles measured from high-resolution hydrodynamical simulations (e.g., Schneider & Robertson 2018) that reproduce this phenomenon could yield helpful comparisons for interpreting observations such as ours.

Future work must compare the range of plausible wind geometries to this and other similar data sets in greater depth. Given the significant evidence that the distribution of Mg II-absorbing material in galactic winds and gaseous halos is characterized by clumpy, small-scale structures (e.g., Monier et al. 1998; Rauch et al. 2002; Rogerson & Hall 2012; Chen et al. 2014; Crighton et al. 2015; Lau et al. 2016; Lopez et al. 2018), such explorations should include models that allow for clumpiness in the wind material (e.g., Schneider et al. 2018; Hummels et al. 2019; Suresh et al. 2019). Gronke et al. (2017) have performed a detailed study of the Lyα spectral profiles predicted by radiative transfer models through winds having numerous small, optically thick clumps along the line of sight. They find that if the number of clumps exceeds a threshold $\gtrsim$10–50, the resulting spectra can be successfully fit with much simpler, homogeneous shell-model geometries, and furthermore that the column densities of the best-fit shells are similar to those of the clumps in total. These results suggest that the simple wind model fitting we adopt here may indeed be yielding columns and mass flow rates that are representative of the physical characteristics of the wind in TKRS 4389. However, any similarity between the line profiles produced by homogeneous versus clumpy winds, as well as any correspondence between the implied column densities of such models, remains to be demonstrated for Mg II.

5.4. TKRS 4389 in Context with Previous Surveys

Finley et al. (2017b) and Feltre et al. (2018) presented Mg II and Fe II emission and absorption results from the MUSE Hubble Ultra Deep Field Survey, where they analyzed these line profiles for a sample of galaxies across the star-forming main sequence (SFMS; Whitaker et al. 2011). Intriguingly, Finley et al. (2017b) found that galaxies that exhibit only emission (and no absorption) in Mg II and those with Fe II* emission occupy separate regions of the SFMS: galaxies with $M_* < 10^9\,M_\odot$ exhibit Mg II emission but no Fe II* emission, and those with $M_* > 10^{10}\,M_\odot$ exhibit Fe II* emission and strong Mg II absorption but no Mg II emission. Galaxies with intermediate masses show emission from both Mg II and Fe II* and tend to have Mg II P Cygni profiles. These authors also found that those galaxies with P Cygni profiles have higher SFR surface densities than those that show pure Mg II emission. Kornei et al. (2013) found in composite spectra that Mg II emitters tend to have higher specific SFRs, lower masses, and less reddening due to dust, the last of which would directly impact photon propagation and thus the emission mechanism. Albeit at higher redshift ($z \sim 2$), Erb et al. (2012) found a similar relationship between galaxy stellar mass and the presence of Mg II emission and absorption. TKRS 4389, with its $M_* = 10^{9.9}\,M_\odot$ and $\Sigma_{\mathrm{SFR}} = 0.956\,M_\odot\,\mathrm{yr}^{-1}\,\mathrm{kpc}^{-2}$ (Rubin et al. 2014), falls into the "intermediate" stellar mass regime identified by Finley et al. (2017b). Its strong P Cygni line profile is typical of such systems, as well as those with comparably high SFR surface densities.

More recently, Henry et al. (2018) studied both Lyα and Mg II line profiles in a sample of "Green Pea" galaxies using a combination of HST/COS and MMT optical spectroscopy. They found that the Mg II line profiles exhibited strong emission and either weak or negligible absorption. In principle, such profiles must be dominated by Mg II line emission from H II regions, as the total equivalent width of absorption plus emission features resulting from pure continuum scattering must sum to zero (in the absence of slit losses and/or dust scattering). Henry et al. (2018) concluded that the observed line profiles are consistent with a picture in which this H II region emission is subject to a modest level of resonant scattering due to the low optical depth of the ISM and outflow material in these very low mass, starbursting systems.

Guseva et al. (2019) analyzed a large sample of low-metallicity, star-forming galaxies observed in the Sloan Digital Sky Survey, selected based on the strength of their Hβ, [O III],

and Mg II emission. They reported that galaxies exhibiting Mg II emission lie above the SFMS (have high SFRs relative to their stellar masses). They attribute this trend to the observed Mg II photons arising from H II regions, where the Mg II emitters have relatively greater recent starburst activity. This finding lends support to similar conclusions reached by Henry et al. (2018) and Feltre et al. (2018) based on photoionization modeling (see also Erb et al. 2012). While our radiative transfer modeling assumes that the extended emission we observe arises from resonant scattering of *continuum* photons by a galactic wind, these previous analyses suggest that some contribution from H II regions is likely in the central galactic regions. Indeed, some excess λ2796 emission is apparent at small distances (<10 kpc) from TKRS 4389 relative to our radiative transfer models; this excess emission may originate from H II regions hosting vigorous star formation.

We note that the Finley et al. (2017b), Feltre et al. (2018), and Henry et al. (2018) studies characterize the Mg II and Fe II emission in a "down-the-barrel" sense, analyzing spectra dominated by the stellar galactic regions and not by emission from the CGM. Drawn from the same galaxy sample, Finley et al. (2017a) reported Fe II* emission extending to a half-light radius of ∼4 kpc around a galaxy whose disk extends to a half-light radius of only 2.5 kpc. In Figure 4 (right), we show Fe II* emission extended ∼7 kpc from the center of TKRS 4389, but we caution that our effective resolution is too poor to properly resolve these scales. Regarding the detection or lack thereof of extended Mg II in the Finley et al. (2017b) sample, we note that their redshift range extends from $z = 0.85$ to 1.50 and peaks at $z \sim 1.05$. Therefore, the higher redshifts alone (relative to the redshift of TKRS 4389 at $z \sim 0.69$) would induce a >5× attenuation of the emission due to cosmological surface brightness dimming.

Only a handful of previous studies have directly assessed the spatial extent and surface brightness of Mg II emission in the regions surrounding galaxies' stellar components. Although they are unable to detect extended emission around individual galaxies, Erb et al. (2012) stacked 33 2D spectra to reveal excess Mg II line emission over the continuum on $\sim 1''$ scales at the 1.5–2σ level. Rickards Vaught et al. (2019) observed five galaxies at $z \sim 0.7$ with narrowband imaging using filters covering the wavelength region of the redshifted Mg II doublet. They did not detect extended Mg II emission to limits of $\sim 6 \times 10^{-19}$ erg s^{-1} cm^{-2} arcsec^{-2}, sufficiently sensitive to detect the TKRS 4389 circumgalactic emission. Three of their four galaxies with high-quality measurements have higher stellar mass than TKRS 4389, while the fourth has similar or slightly lower stellar mass. This object, however, has an SFR approximately 1/5 that of TKRS 4389, and its lack of detection fits a scenario where CGM Mg II emission may be anticorrelated with galaxy mass (at least above some mass) but correlated with SFR. As discussed above, similar trends are exhibited by the Mg II coincident with star-forming regions (i.e., not in the CGM).

A difference in geometry may also have an effect, as Rickards Vaught et al. (2019) suggest that anisotropy may reduce the emission below their detection limits. Our modeling strongly suggests an isotropic wind around TKRS 4389, but this is likely not a generic characteristic given the biconical geometries implied by absorption-line studies (e.g., Kacprzak et al. 2012). Like Rubin et al. (2011), Martin et al. (2013) used slit spectroscopy to observe extended Mg II emission around a high-SFR galaxy, reporting spatially asymmetric extended Mg II to ∼12 kpc. Another such extreme galaxy was observed by Rupke et al. (2019), who have presented the sole 2D high-S/N map of extended Mg II emission to date. Their target was an exceptionally bright compact starburst with a stellar mass $\log M_*/M_\odot = 11.1$ and an SFR = 100–200 $M_\odot$ yr^{-1}. Like TKRS 4389, this system is a merger remnant, exhibiting faint tidal tail signatures in deep HST imaging. Their mapping revealed Mg II emission extending to ≈ 10 kpc from this system, as well as bright [O II] emission extending five times farther (to ≈ 50 kpc). The [O II] emission exhibits an hourglass shape suggestive of evacuated, bipolar bubbles, whereas the Mg II exhibits a significantly more irregular morphology. Both this and the Martin et al. (2013) target are more similar to TKRS 4389 than most of the Rickards Vaught et al. (2019) sample, which fits the stellar mass and SFR dependence picture outlined above. However, the radically different morphologies imply that while one may expect to observe galactic winds via extended Mg II for galaxies of certain properties (e.g., M_* and SFR), they likely possess diverse geometries.

6. Conclusions

We have presented the first observations from our integral field spectroscopy survey of Mg II emission and absorption from galactic winds in and around star-forming galaxies. Our target, TKRS 4389, is a starbursting galaxy merger at $z = 0.69$ with a stellar mass $\log M_*/M_\odot = 9.9$ and SFR = 50 M_* yr^{-1}. Our spatially resolved spectroscopy reaches a 1σ surface brightness limit of 4.8×10^{-19} erg s^{-1} cm^{-2} arcsec^{-2} measured over a 5 Å wide spectral region, enabling the first map of extended Mg II emission on scales extending >10 kpc from stellar galactic regions. From our measurements of the spatial distributions of Mg II and Fe II* emission, analysis of the spectral line profiles, and 3D radiative transfer modeling, we report the following key results:

1. We discover significant (at the 3σ level above our surface brightness limit) Mg II λ2796 emission arising from the CGM and extending $\gtrsim$15 kpc from the galaxy disk. From the surface brightness contours alone, we measure a total extent of 37 ± 3 kpc, while we estimate a ∼31 kpc total extent along the minor axis after deconvolving with the 1.″6 seeing.
2. In spaxels covering the galaxy disk, where stellar continuum is evident, we observe the characteristic P Cygni absorption/emission profile of gaseous outflows in Mg II, but this feature gives way to full emission in spaxels off the galaxy disk. The emission extends in all directions from the galaxy, i.e., not simply along the minor axis, suggesting that the outflowing wind is isotropic.
3. On the galaxy, our data show absorption in the resonant Fe II transitions and emission from nonresonant Fe II* transitions. However, the Fe II* emission is not significantly extended as is the Mg II, having a 3σ extent of <7 kpc from the galaxy and consistent with the derived seeing FWHM.
4. We have generated a suite of 3D radiative transfer models of galactic outflows and rebinned and convolved the model output both spatially and spectrally to match the KCWI

observations. By fitting each model to the data in three dimensions, we find that isotropic outflow models with radially declining velocity profiles and extents >20 kpc are favored. Among the two density profiles we test ($n \propto r^{-1}$ and $\propto r^{-2}$), the former provides a closer match to the observed emission profile.

5. Our modeling most disfavors biconical winds with small opening angles, those with radially increasing ($v \propto r$) velocity profiles, those with $n \propto r^{-2}$ density profiles, and those with radial extents $r \leqslant 10$ kpc.
6. Independent of our resonantly scattered outflow models, we considered alternate scenarios in which collisional excitation and/or radiative recombination give rise to our detected Mg II signal. The expected surface brightnesses from these mechanisms fall short of that observed by factors of $\sim$2–10^5 depending on the assumed hydrogen density, further supporting the resonant scattering origin.
7. Our preferred wind geometry, extent, and velocity and density profiles imply a mass outflow rate of $\sim 55\, M_{\odot}\, \mathrm{yr}^{-1}$ at $r = 25$ kpc. This mass outflow is approximately equal to the TKRS 4389 SFR $\sim 50\, M_{\odot}\, \mathrm{yr}^{-1}$, resulting in a mass-loading factor of $\eta \sim 1$ at this radius. We posit that this material is unlikely to escape the galaxy's potential well, as the velocity of our best-fit model wind at $r = 25$ kpc (50 km s^{-1}) falls well below the escape speed expected for the galaxy halo.

The observations presented herein represent one of the first reported integral field spectroscopic maps of extended Mg II emission, and they will be followed by a larger survey spanning galaxy stellar mass and SFR. These direct constraints on outflow morphology and extent should inform both subgrid feedback prescriptions employed in cosmological simulations and more detailed theoretical studies of outflow mechanisms themselves. As the KCWI and MUSE IFUs have become workhorse instruments on 10 m class telescopes, further insights will no doubt follow from similar studies, as resonantly scattered photons in outflowing winds provide beacons of this fundamental evolutionary activity in galaxies.

The authors wish to recognize and acknowledge the very significant cultural role and reverence that the summit of Maunakea has always had within the indigenous Hawaiian community. We are most fortunate to have the opportunity to conduct observations from this mountain. The data presented herein were obtained at the W. M. Keck Observatory, which is operated as a scientific partnership among the California Institute of Technology, the University of California, and the National Aeronautics and Space Administration. The Observatory was made possible by the generous financial support of the W. M. Keck Foundation. We would like to thank Brice Ménard, Bill Mathews, and David Koo for helpful discussions, as well as Zheng Cai for guidance on the data reduction and analysis. Support for this work was provided by NASA through grant number HST-GO-13300.005-A from the Space Telescope Science Institute, which is operated by AURA, Inc., under NASA contract NAS 5-26555.

Facility: Keck(KCWI).

Software: KDERP (https://github.com/Keck-DataReductionPipelines/KcwiDRP)
linetools (https://github.com/linetools)
astropy (Astropy Collaboration et al. 2013)
reproject (https://reproject.readthedocs.io/en/stable).

ORCID iDs

Joseph N. Burchett https://orcid.org/0000-0002-1979-2197
Kate H. R. Rubin https://orcid.org/0000-0001-6248-1864
J. Xavier Prochaska https://orcid.org/0000-0002-7738-6875
Alison L. Coil https://orcid.org/0000-0002-2583-5894
Ryan Rickards Vaught https://orcid.org/0000-0001-9719-4080
Joseph F. Hennawi https://orcid.org/0000-0002-7054-4332

References

Armillotta, L., Fraternali, F., & Marinacci, F. 2016, MNRAS, 462, 4157
Astropy Collaboration, Robitaille, T. P., Tollerud, E. J., et al. 2013, A&A, 558, A33
Baron, D., Netzer, H., Prochaska, J. X., et al. 2018, MNRAS, 480, 3993
Barro, G., Pérez-González, P. G., Gallego, J., et al. 2011, ApJS, 193, 13
Bolatto, A. D., Warren, S. R., Leroy, A. K., et al. 2013, Natur, 499, 450
Bordoloi, R., Lilly, S. J., Knobel, C., et al. 2011, ApJ, 743, 10
Bordoloi, R., Rigby, J. R., Tumlinson, J., et al. 2016, MNRAS, 458, 1891
Carr, C., Scarlata, C., Panagia, N., & Henry, A. 2018, ApJ, 860, 143
Chen, H.-W., Gauthier, J.-R., Sharon, K., et al. 2014, MNRAS, 438, 1435
Chisholm, J., Tremonti, C. A., Leitherer, C., & Chen, Y. 2017, MNRAS, 469, 4831
Chisholm, J., Tremonti Christy, A., Leitherer, C., & Chen, Y. 2016, MNRAS, 463, 541
Cicone, C., Maiolino, R., Sturm, E., et al. 2014, A&A, 562, A21
Coil, A. L., Weiner, B. J., Holz, D. E., et al. 2011, ApJ, 743, 46
Corlies, L., Peeples, M. S., Tumlinson, J., et al. 2020, ApJ, 896, 125
Cowie, L. L., McKee, C. F., & Ostriker, J. P. 1981, ApJ, 247, 908
Crighton, N. H. M., Hennawi, J. F., & Prochaska, J. X. 2013, ApJL, 776, L18
Crighton, N. H. M., Hennawi, J. F., Simcoe, R. A., et al. 2015, MNRAS, 446, 18
Erb, D. K., Quider, A. M., Henry, A. L., & Martin, C. L. 2012, ApJ, 759, 26
Feltre, A., Bacon, R., Tresse, L., et al. 2018, A&A, 617, A62
Ferland, G. J., Chatzikos, M., Guzmán, F., et al. 2017, RMxAA, 53, 385
Fielding, D., Quataert, E., McCourt, M., & Thompson, T. A. 2017, MNRAS, 466, 3810
Finley, H., Bouché, N., Contini, T., et al. 2017a, A&A, 605, A118
Finley, H., Bouché, N., Contini, T., et al. 2017b, A&A, 608, A7
Fiore, F., Feruglio, C., Shankar, F., et al. 2017, A&A, 601, A143
Fraternali, F., & Binney, J. J. 2006, MNRAS, 366, 449
Geach, J. E., Hickox, R. C., Diamond-Stanic, A. M., et al. 2014, Natur, 516, 68
Giavalisco, M., Ferguson, H. C., Koekemoer, A. M., et al. 2004, ApJL, 600, L93
Gronke, M., Dijkstra, M., McCourt, M., & Peng Oh, S. 2017, A&A, 607, A71
Gronke, M., & Oh, S. P. 2018, MNRAS, 480, L111
Guseva, N. G., Izotov, Y. I., Fricke, K. J., & Henkel, C. 2019, A&A, 624, A21
Haardt, F., & Madau, P. 1996, ApJ, 461, 20
Harrison, C. M., Alexander, D. M., Swinbank, A. M., et al. 2012, MNRAS, 426, 1073
Heckman, T. M., Alexandroff, R. M., Borthakur, S., Overzier, R., & Leitherer, C. 2015, ApJ, 809, 147
Heckman, T. M., Armus, L., & Miley, G. K. 1987, AJ, 93, 276
Heckman, T. M., Lehnert, M. D., Strickland, D. K., & Armus, L. 2000, ApJS, 129, 493
Henry, A., Berg, D. A., Scarlata, C., Verhamme, A., & Erb, D. 2018, ApJ, 855, 96
Hummels, C. B., Smith, B. D., Hopkins, P. F., et al. 2019, ApJ, 882, 156
Kacprzak, G. G., Churchill, C. W., & Nielsen, N. M. 2012, ApJL, 760, L7
Kasen, D., Thomas, R. C., & Nugent, P. 2006, ApJ, 651, 366
Kornei, K. A., Shapley, A. E., Martin, C. L., et al. 2012, ApJ, 758, 135
Kornei, K. A., Shapley, A. E., Martin, C. L., et al. 2013, ApJ, 774, 50
Lau, M. W., Prochaska, J. X., & Hennawi, J. F. 2016, ApJS, 226, 25
Lehnert, M. D., Heckman, T. M., & Weaver, K. A. 1999, ApJ, 523, 575
Leroy, A. K., Walter, F., Martini, P., et al. 2015, ApJ, 814, 83
Leslie, S. K., Bryant, J. J., Ho, I. T., et al. 2017, MNRAS, 471, 2438
Leung, G. C. K., Coil, A. L., Azadi, M., et al. 2017, ApJ, 849, 48
Lopez, S., Tejos, N., Ledoux, C., et al. 2018, Natur, 554, 493
Lutz, D., Sturm, E., Janssen, A., et al. 2020, A&A, 633, A134
Maller, A. H., & Bullock, J. S. 2004, MNRAS, 355, 694
Martin, C. L. 2005, ApJ, 621, 227
Martin, C. L., & Bouché, N. 2009, ApJ, 703, 1394
Martin, C. L., Shapley, A. E., Coil, A. L., et al. 2012, ApJ, 760, 127
Martin, C. L., Shapley, A. E., Coil, A. L., et al. 2013, ApJ, 770, 41

McCourt, M., Oh, S. P., O'Leary, R., & Madigan, A.-M. 2018, MNRAS, 473, 5407
McKinley, B., Tingay, S. J., Carretti, E., et al. 2018, MNRAS, 474, 4056
Monier, E. M., Turnshek, D. A., & Lupie, O. L. 1998, ApJ, 496, 177
Morrissey, P., Matuszewski, M., Martin, D. C., et al. 2018, ApJ, 864, 93
Moster, B. P., Naab, T., & White, S. D. M. 2013, MNRAS, 428, 3121
Muratov, A. L., Kereš, D., Faucher-Giguère, C.-A., et al. 2015, MNRAS, 454, 2691
Muratov, A. L., Kereš, D., Faucher-Giguère, C.-A., et al. 2017, MNRAS, 468, 4170
Murray, N., Ménard, B., & Thompson, T. A. 2011, ApJ, 735, 66
Murray, N., Quataert, E., & Thompson, T. A. 2010, ApJ, 709, 191
Nelson, D., Pillepich, A., Springel, V., et al. 2019, MNRAS, 490, 3234
Oppenheimer, B. D., & Davé, R. 2006, MNRAS, 373, 1265
Pettini, M., Shapley, A. E., Steidel, C. C., et al. 2001, ApJ, 554, 981
Planck Collaboration, Ade, P. A. R., Aghanim, N., et al. 2016, A&A, 594, A13
Prochaska, J. X., Kasen, D., & Rubin, K. 2011, ApJ, 734, 24
Ptak, A., Mobasher, B., Hornschemeier, A., Bauer, F., & Norman, C. 2007, ApJ, 667, 826
Ragagnin, A., Dolag, K., Moscardini, L., Biviano, A., & D'Onofrio, M. 2019, MNRAS, 486, 4001
Rahmati, A., Pawlik, A. H., Raičević, M., & Schaye, J. 2013, MNRAS, 430, 2427
Rauch, M., Sargent, W. L. W., & Barlow, T. A. 1999, ApJ, 515, 500
Rauch, M., Sargent, W. L. W., Barlow, T. A., & Simcoe, R. A. 2002, ApJ, 576, 45
Rickards Vaught, R. J., Rubin, K. H. R., Arrigoni Battaia, F., Prochaska, J. X., & Hennawi, J. F. 2019, ApJ, 879, 7
Robitaille, T. P., Rossa, J., Bomans, D. J., & van der Marel, R. P. 2007, A&A, 464, 541
Rogerson, J. A., & Hall, P. B. 2012, MNRAS, 421, 971
Rubin, K. H. R., Prochaska, J. X., Koo, D. C., et al. 2014, ApJ, 794, 156
Rubin, K. H. R., Prochaska, J. X., Koo, D. C., & Phillips, A. C. 2012, ApJL, 747, L26
Rubin, K. H. R., Prochaska, J. X., Koo, D. C., Phillips, A. C., & Weiner, B. J. 2010, ApJ, 712, 574
Rubin, K. H. R., Prochaska, J. X., Ménard, B., et al. 2011, ApJ, 728, 55
Rupke, D. S., Veilleux, S., & Sanders, D. B. 2005a, ApJS, 160, 87
Rupke, D. S., Veilleux, S., & Sanders, D. B. 2005b, ApJS, 160, 115
Rupke, D. S. N., Coil, A., Geach, J. E., et al. 2019, Natur, 574, 643
Rupke, D. S. N., & Veilleux, S. 2013, ApJ, 768, 75
Rupke, D. S. N., & Veilleux, S. 2015, ApJ, 801, 126
Sanders, D. B., & Mirabel, I. F. 1996, ARA&A, 34, 749
Savage, B. D., & Sembach, K. R. 1996, ARA&A, 34, 279
Scarlata, C., & Panagia, N. 2015, ApJ, 801, 43
Schneider, E. E., & Robertson, B. E. 2018, ApJ, 860, 135
Schneider, E. E., Robertson, B. E., & Thompson, T. A. 2018, ApJ, 862, 56
Sharp, R. G., & Bland-Hawthorn, J. 2010, ApJ, 711, 818
Sobolev, V. V. 1960, Moving Envelopes of Stars (Cambridge, MA: Harvard Univ. Press)
Sravan, N., Faucher-Giguère, C.-A., van de Voort, F., et al. 2016, MNRAS, 463, 120
Steidel, C. C., Adelberger, K. L., Shapley, A. E., et al. 2003, ApJ, 592, 728
Steidel, C. C., Erb, D. K., Shapley, A. E., et al. 2010, ApJ, 717, 289
Suresh, J., Nelson, D., Genel, S., Rubin, K. H. R., & Hernquist, L. 2019, MNRAS, 483, 4040
Thompson, T. A., Fabian, A. C., Quataert, E., & Murray, N. 2015, MNRAS, 449, 147
Thompson, T. A., Quataert, E., Zhang, D., & Weinberg, D. H. 2016, MNRAS, 455, 1830
Tremonti, C. A., Heckman, T. M., Kauffmann, G., et al. 2004, ApJ, 613, 898
Tremonti, C. A., Moustakas, J., & Diamond-Stanic, A. M. 2007, ApJL, 663, L77
van de Voort, F., & Schaye, J. 2013, MNRAS, 430, 2688
Veilleux, S., Maiolino, R., Bolatto, A. D., & Aalto, S. 2020, A&A Rv, 28, 2
Veilleux, S., Meléndez, M., Sturm, E., et al. 2013, ApJ, 776, 27
Veilleux, S., Shopbell, P. L., Rupke, D. S., Bland-Hawthorn, J., & Cecil, G. 2003, AJ, 126, 2185
Walter, F., Weiss, A., & Scoville, N. 2002, ApJL, 580, L21
Weiner, B. J., Coil, A. L., Prochaska, J. X., et al. 2009, ApJ, 692, 187
Weiner, B. J., Phillips, A. C., Faber, S. M., et al. 2005, ApJ, 620, 595
Weiß, A., Walter, F., Neininger, N., & Klein, U. 1999, A&A, 345, L23
Whitaker, K. E., Labbé, I., van Dokkum, P. G., et al. 2011, ApJ, 735, 86
Willmer, C. N. A., Faber, S. M., Koo, D. C., et al. 2006, ApJ, 647, 853
Wirth, G. D., Willmer, C. N. A., Amico, P., et al. 2004, AJ, 127, 3121
Yoshida, M., Yagi, M., Ohyama, Y., et al. 2016, ApJ, 820, 48